

Cite this: *Phys. Chem. Chem. Phys.*, 2011, **13**, 18705–18723

www.rsc.org/pccp

PERSPECTIVE

# Deceleration of supersonic beams using inhomogeneous electric and magnetic fields

Stephen D. Hogan, Michael Motsch and Frédéric Merkt\*

Received 27th May 2011, Accepted 19th July 2011

DOI: 10.1039/c1cp21733j

Methods for the production of cold atomic and molecular samples relying on the deceleration of pulsed supersonic beams are described and a review of the corresponding literature is presented. These methods include multistage Stark deceleration, multistage Zeeman deceleration, and Rydberg–Stark deceleration. Recent applications of the cold samples produced with these techniques are summarized.

## 1 Introduction

This article is devoted to a review of methods for the deceleration of pulsed supersonic beams, that can be used to produce dense, cold atomic and molecular samples in slow beams or in electric or magnetic traps. The development of these methods is part of a larger effort, by chemists and physicists, directed toward studying the properties of molecules at temperatures below 1 K. This effort is motivated by the prospects of (i) investigating chemical processes close to the absolute zero-point temperature<sup>1</sup> where reaction rates and product states are expected to be strongly influenced by resonance and tunneling phenomena,<sup>2</sup> long-range interactions between the reactants, hyperfine effects, nuclear-spin symmetry<sup>3,4</sup> and external fields,<sup>5</sup> (ii) carrying out precision measurements of energy intervals which may permit observation of properties revealing very weak symmetry-violating interactions such as a possible electric dipole moment of the electron,<sup>6</sup> energy differences between two enantiomers of a chiral molecule,<sup>7,8</sup> or even reveal a possible time dependence of fundamental constants,<sup>9</sup> (iii) studying dipole–dipole interactions in molecular gases close to quantum degeneracy<sup>3</sup> or dipole–dipole and many-body interactions in frozen Rydberg gases,<sup>10</sup> with applications in the realization of quantum gates,<sup>11,12</sup> and (iv) studying the properties of ultracold atoms and molecules in the vicinity of cryogenic chip-based devices.<sup>13–15</sup> Several review articles which describe this effort in the context of recent or proposed experiments involving cold molecules have been published lately.<sup>2,16–21</sup>

The deceleration methods that are at the focus of the present article rely on supersonic expansions as a means to generate cold, dense samples of atoms and molecules. They exploit spatially inhomogeneous and time-varying electric and magnetic fields to slow down a subset of the particles in the supersonic beam having specific phase-space characteristics and being in a

selected quantum state. After deceleration one attains cold (translational temperature of less than 1 K) samples of state-selected atoms or molecules. Such samples can either be used directly, for instance in a high-resolution spectroscopic measurement or a reaction dynamics experiment, or as a starting sample for further cooling. While the present article is restricted to the description and use of methods for the deceleration of pulsed supersonic beams, it is important to realize that such methods only form a subclass of techniques that are currently being developed to generate and study cold molecules. Other methods include cold molecule formation by photoassociation<sup>22</sup> and magnetoassociation<sup>23,24</sup> of ultracold atoms, buffergas cooling<sup>25</sup> or sympathetic cooling using laser-cooled ions as a low-temperature thermal bath,<sup>26–28</sup> deceleration using optical fields,<sup>29</sup> expansion from a rotating nozzle,<sup>30</sup> filtering the low velocity tail of an effusive beam,<sup>31</sup> and in favorable cases laser cooling.<sup>32–34</sup> Information on these methods can be found in the review articles cited above and in many articles of this special issue. The method of deceleration using optical fields, though also applicable to supersonic beams, is not discussed in detail and we refer the reader to the original literature.<sup>29,35,36</sup>

The use of inhomogeneous magnetic and electric fields to exert forces on gas-phase particles has a long and rich history in atomic and molecular physics, and can be broadly divided into three successive phases. During the first phase, the forces were used to act on atomic samples in well-collimated thermal (effusive) beams. This phase started with the experiments of Gerlach and Stern which led to the experimental demonstration of space quantization.<sup>37–41</sup> In these pioneering atom-optics experiments, inhomogeneous magnetic fields were used to separate a beam of silver atoms into its magnetic components ( $m_s = \pm 1/2$ ) and to demonstrate the possibility of measuring magnetic moments. The extension of this beam method to measure nuclear magnetic moments by Rabi and his coworkers<sup>42,43</sup> can be regarded as a key step towards the establishment of nuclear magnetic resonance spectroscopy (see reviews by Bloch and Rabi,<sup>44</sup> or Emsley and Feeney<sup>45</sup>).

ETH Zürich, Laboratorium für Physikalische Chemie,  
Wolfgang-Pauli-Strasse 10, CH-8093 Zurich, Switzerland

The second phase was initiated by the realization that very dense, cold samples can be produced in supersonic beams.<sup>46,47</sup> These properties, and the collision-free environment that they provide, make supersonic beams ideally suited to spectroscopic and reaction dynamics experiments with the result that supersonic beams rapidly became one of the main experimental tools of gas-phase physical chemistry and molecular physics (see ref. 48–50 and references therein). Motivated by spectroscopic and reaction-dynamics experiments, the need arose to exploit the forces generated by inhomogeneous fields to prepare, guide and focus molecules in selected internal quantum states. During this second phase, inhomogeneous field distributions were primarily used to control the *transverse* motion of the supersonic beams, exploiting state-specific focussing and defocussing forces<sup>51–55</sup> to achieve high-densities of quantum-state-selected molecules.

This article presents a review of the third phase in the use of inhomogeneous electric and magnetic fields in which efforts are invested to also control the *longitudinal* motion of the gas-phase particles in supersonic beams, *i.e.*, the motion along the direction of propagation of the beams. The first experiments to achieve this goal were carried out by Bethlem, Meijer and co-workers who demonstrated the phase-stable deceleration of state-selected CO and ND<sub>3</sub> molecules using inhomogeneous electric fields to form dense samples of these molecules in slow beams or at rest in the laboratory-fixed frame of reference<sup>16, 56, 57</sup>, with obvious potential applications in high-resolution spectroscopy and reaction dynamics. By so doing, they established a powerful method, now known as “multistage Stark deceleration”, to produce cold dense samples of polar molecules. They could rightly claim to have “tamed” molecular beams.<sup>58</sup> Their method was extended to (i) decelerate paramagnetic species by multistage Zeeman deceleration using inhomogeneous magnetic fields<sup>59,60</sup> and (ii) decelerate atoms and molecules in Rydberg states by Rydberg–Stark deceleration.<sup>61–63</sup> While deceleration experiments are the most relevant in the context of studies of cold atomic and molecular samples, experiments have also been carried out<sup>64,65</sup> or proposed<sup>66</sup> in which the inhomogeneous fields serve the purpose of accelerating the particles.

The three types of neutral-particle-beam decelerators mentioned above are depicted schematically in Fig. 1. Common to all three is the use of a pulsed valve to generate a supersonic expansion and a skimmer to select the coldest, densest central part of the beam. The particles to be decelerated are usually added in small quantities to a rare gas which acts as a carrier gas in the supersonic expansion. Typical beam velocities of the particles depend on the carrier gas and range from about 300 m s<sup>−1</sup> (xenon) to about 2000 m s<sup>−1</sup> (helium) when the expansion occurs from a reservoir held at room temperature. Typically, nozzle stagnation pressures of 1 bar or more are used. The decelerators, which will be described in more detail in Sections 2.2 and 2.3, are placed downstream from the skimmer and their design characteristics depend upon the initial velocity of the beam, on the mass of the particles to be decelerated and on their electric and magnetic properties, *i.e.*, their Stark and Zeeman effects. Because of the strong cooling that takes place in the supersonic expansion, only the lowest rotational levels of the ground vibrational level of the ground electronic state are populated—at least for small molecules.

The general physical principles of these acceleration/deceleration experiments are the same as those exploited by Gerlach and Stern. In the presence of electric and magnetic fields, the energy levels of an atom or a molecule are shifted according to the Stark and Zeeman effects, with the shifts known as Stark shifts and Zeeman shifts, respectively. The Stark shifts display a linear or a quadratic dependence on the electric field strength  $|\vec{F}|$  at low fields, depending on whether the quantum states coupled by the field are degenerate or not. The Zeeman shifts tend to be linear at low magnetic field strength  $|\vec{B}|$ , the magnetic field having the effect of lifting the degeneracy of the magnetic sublevels in free space. Quantum systems undergoing a linear Stark or Zeeman effect can be thought of as having an electric ( $\vec{\mu}_{\text{el}}$ ) or magnetic ( $\vec{\mu}_{\text{mag}}$ ) dipole moment which directly couples to the applied external electric ( $\vec{F}$ ) or magnetic ( $\vec{B}$ ) field. The linear energy shifts can be expressed as

$$E_{\text{S}} = -\vec{\mu}_{\text{el}} \cdot \vec{F}, \quad E_{\text{Z}} = -\vec{\mu}_{\text{mag}} \cdot \vec{B}. \quad (1)$$

A quantum state the energy of which is lowered (raised) in the presence of a field is often referred to as a “red-shifted” (“blue-shifted”) state, or a “high-field-seeking” (“low-field-seeking”) state. The latter designation can be understood from the fact that particles undergoing a Stark or a Zeeman effect are subject to a force  $\vec{f}$  in an inhomogeneous field

$$\vec{f}_{\text{S}} = -\nabla E_{\text{S}}, \quad \vec{f}_{\text{Z}} = -\nabla E_{\text{Z}} \quad (2)$$

which is proportional to the field gradient. In inhomogeneous fields, particles in low(high)-field-seeking states are accelerated in the direction of decreasing (increasing) field strength. If the force is perpendicular to the beam propagation axis, it can be exploited to deflect a beam or split it into different components, as in the experiments of Gerlach and Stern. If the acceleration vector points in the direction parallel or antiparallel to the beam propagation axis, the particles in the beam are accelerated or decelerated longitudinally. The magnetic moments associated with nuclear spins are much smaller than those arising from electron spins so that the forces originating from the nuclear Zeeman effect are to a good approximation negligible compared to those arising from the electron Zeeman effect. Because it is not possible to generate an electric or magnetic field distribution with a local maximum in free space, low-field-seeking states are the most suitable for deceleration experiments. Deceleration of molecules in high-field-seeking states requires more advanced schemes such as alternating gradient (ag) deceleration,<sup>67</sup> which have been discussed in detail by Bethlem and Meijer<sup>16</sup> and Tarbutt *et al.*<sup>6</sup> and are not discussed here.

As illustrations of concrete atomic and molecular systems that can be produced at low temperature using these deceleration methods, Fig. 2 depicts the Stark effect in the ground state of a polar molecule (OH, panel (a)), the Zeeman effect in the ground state of atomic hydrogen (panel (b)) and in the ground rotational level ( $N = 1$ ) of molecular oxygen, which splits into three components with  $J = 0, 1$  and  $2$  at zero field because of the magnetic interaction between the rotational and electron-spin motions. The fourth panel (d) depicts the Stark effect in Rydberg states with the example of the hydrogen atom. The low-field-seeking states, which are particularly suited to deceleration experiments, are indicated as dashed curves in each case. The ranges

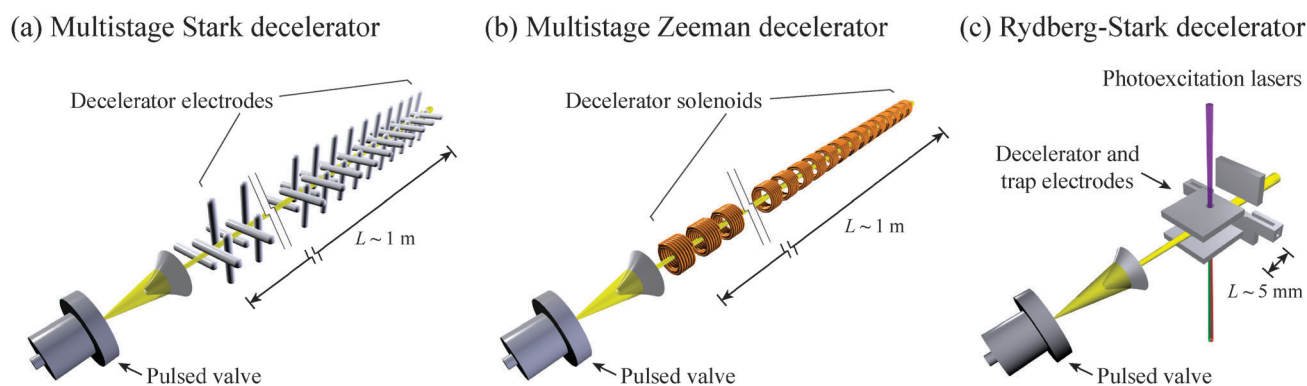


**Fig. 1** Schematic diagrams of (a) a multistage Stark decelerator, (b) a multistage Zeeman decelerator and (c) a single-stage Rydberg–Stark decelerator and trap.

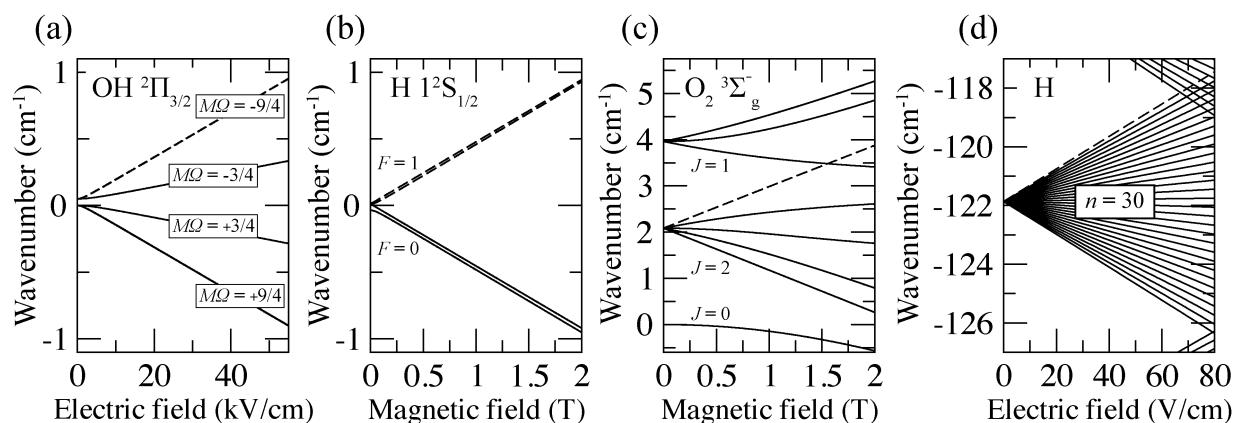


**Fig. 2** (a) The Stark effect in the  $2\Pi_{3/2}$  ground state of OH, the Zeeman effect in (b) the  $1^2S_{1/2}$  ground state of the hydrogen atom and (c) the  $3\Sigma_g^-$  ground state of  $O_2$ , and (d) the Stark effect in the  $n = 30$ ,  $m_l = 0$  Rydberg state of atomic hydrogen. Low-field-seeking states most suitable for deceleration are indicated by dashed curves.

of electric and magnetic fields considered in the figure correspond roughly to those that are used in experiments, *i.e.*, up to about  $100 \text{ kV cm}^{-1}$  and  $2 \text{ T}$  in multistage Stark and Zeeman deceleration, respectively (see Fig. 2(a)–(c)). The corresponding Stark and Zeeman shifts are similar and lie in the range of  $1$  to  $2 \text{ cm}^{-1}$ . Because of the very large dipole moments exhibited by Rydberg states, their Stark shifts are much larger and amount to about  $4 \text{ cm}^{-1}$  at field strengths of  $\sim 65 \text{ V cm}^{-1}$  at  $n \approx 30$ .

Given that the kinetic energy of a particle of mass number  $N_M$  moving at a velocity of  $400 \text{ m s}^{-1}$  amounts to

$$E_{\text{kin}}/(hc \text{ cm}^{-1}) = 6.7 N_M, \quad (3)$$

one can immediately conclude that, while a single deceleration stage may be sufficient to completely decelerate a beam of Rydberg atoms or molecules, the complete deceleration of a beam of polar molecules with electric fields and of paramagnetic atoms and molecules with magnetic fields necessitates many successive deceleration stages (of the order of  $10$  to  $100$ ). The Stark deceleration of polar molecules and the Zeeman deceleration of paramagnetic species thus possess many common features and will thus be described jointly in Section 2.2. The deceleration of Rydberg atoms and molecules typically involves a single deceleration stage and requires the photoexcitation of the atoms or molecules in the beam to Rydberg states prior to

deceleration. Rydberg–Stark deceleration thus requires a different experimental approach, presented in Section 2.3.

Table 1 provides an overview of the cold atomic and molecular samples that have been produced by these deceleration methods. While the variety of the samples is still rather restricted, it is rapidly increasing. Deceleration of supersonic beams is not a goal per se, but opens up an increasing number of scientific applications, primarily in the fields of high-resolution spectroscopy and chemical reaction dynamics. After an initial phase in which the attention was largely focused on technical developments, these methods have reached the stage where interesting scientific applications are becoming possible. It thus appears timely to summarize the knowledge acquired so far and outline current and future applications of the cold atomic and molecular samples that can be produced.

## 2 Deceleration techniques

### 2.1 Supersonic beams

Supersonic beams,<sup>48,95–99</sup> the starting point for the techniques discussed herein, are formed by the adiabatic expansion of a gas from a high-pressure reservoir into vacuum through an opening which is large compared to the mean free path of the sample in the high-pressure region. In the expansion, thermal

**Table 1** Species prepared by multistage Stark deceleration (denoted Stark), multistage Zeeman deceleration (denoted Zeeman) and Rydberg–Stark deceleration (denoted Rydberg) of pulsed supersonic beams

Method	Species	State	Remarks	Ref.
Stark	CO	$a^3\Pi_1$	Deceleration	56
		$a^3\Pi_1$	Ag deceleration	67
		$a^3\Pi_1, a^3\Pi_2$	Electric trapping	68
		$a^3\Pi_1$	Chip decelerator	15
		$a^3\Pi_1$	Ring decelerator	69
	$^{13}\text{CO}$	$a^3\Pi_1$	Wire decelerator	70
	$\text{ND}_3$	$\tilde{X}^1A_1$	Electric trapping	71
		$\tilde{X}^1A_1$	Ac trapping	72
	OH	$X^2\Pi_{3/2}$	Deceleration	73
		$X^2\Pi_{3/2}$	Electric trapping	74
		$X^2\Pi_{3/2}$	Magnetic trapping	75
	$\text{SO}_2$	$\tilde{X}^1A_1$	Deceleration	76
	$\text{H}_2\text{CO}$	$\tilde{X}^1A_1$	Deceleration	77
	NH	$a^1\Delta$	Deceleration	78
		$a^1\Delta$	Electric trapping	79
	LiH	$X^1\Sigma^+$	Deceleration	80, 81
	CaF	$X^2\Sigma^+$	Deceleration	80, 81
	YbF	$X^2\Sigma^+$	Ag deceleration	83
	$\text{C}_6\text{H}_5\text{CN}$	$S_0$	Ag deceleration	84
Zeeman	H	$1^2S_{1/2}, F = 1$	Deceleration	59
		$1^2S_{1/2}, F = 1$	Magnetic trapping	85
		$1^2S_{1/2}, F = 3/2$	Deceleration	86
	D	$1^2S_{1/2}, F = 3/2$	Magnetic trapping	87
		$(2p)^5(3s)^1\ ^3P_2$	Deceleration	60
Rydberg	Ar	$(3p)^5(4s)^1\ ^3P_1$	Guiding	88
	$\text{O}_2$	$X\ ^3\Sigma_g^-$	Deceleration	89
	Ar	$n = 15\text{--}25$	Deceleration	90
		$n = 20\text{--}25$	Deceleration	91
		$n = 20\text{--}40$	2D trapping	92
	$\text{H}_2$	$n = 30$	3D trapping	93
		$n = 17$	Deceleration	61
		$n = 21\text{--}40$	Trapping	94

energy in all degrees of freedom—translational, rotational and vibrational—is converted into kinetic energy along the propagation direction of the beam. The result of the expansion is a dense, translationally and internally cold sample moving at high velocity in the laboratory-fixed reference frame. Since it is not possible to increase the phase-space density of a gas using only conservative forces, it is necessary to start with a sample of high initial phase-space density when the aim is to produce high density samples of slow and cold molecules by deceleration. In the following, the equations describing supersonic free jets are briefly summarized. These equations describe continuous expansions accurately and are often also used to estimate typical properties of pulsed supersonic beams despite the clear differences between the two (see for example Miller<sup>95</sup> for more detail in this regard).

Assuming ideal adiabatic expansion from a gas reservoir at a temperature  $T_0$  into vacuum, the terminal stream velocity  $v_t$  of a gas of particles of mass  $m$  and ratio of heat capacity at constant pressure to that at constant volume of  $\gamma = C_p/C_v$ , is given by

$$v_t = \sqrt{\frac{\gamma}{\gamma - 1}} \sqrt{\frac{2kT_0}{m}}. \quad (4)$$

The longitudinal velocity distribution of a beam of this kind is

$$f(v_z)dv_z = N^{-1}v_z^2 \exp\left(-\frac{(v_z - v_t)^2}{2\sigma_v^2}\right)dv_z, \quad (5)$$

where  $\sigma_v^2 = \frac{kT_t}{m}$  is related to the terminal temperature  $T_t$  of the beam, and  $N = \sqrt{2\pi\sigma_v(\sigma_v^2 + v_t^2)}$  is a normalization constant. A low temperature  $T_t$  corresponds to a narrow longitudinal velocity distribution. For  $\sigma_v \ll v_t$ , the approximation that  $N^{-1}v_z^2 \approx (\sqrt{2\pi}\sigma_v)^{-1}$  can be made in eqn (5).

To characterize the expansion process and obtain the thermodynamic properties of the supersonic beam, the Mach number  $M = v_s/a$  is introduced, which relates the instantaneous stream velocity  $v_s$  to the local speed of sound in the beam,  $a = \sqrt{\frac{\gamma kT}{m}}$ . The dependence of the Mach number on the distance  $z$  from the nozzle can be expressed as

$$M(z) = A(z/d - B)^{\gamma-1} - \frac{1}{2} \left( \frac{\gamma+1}{\gamma-1} \right) \frac{1}{A} (z/d - B)^{1-\gamma}, \quad (6)$$

where  $d$  is the diameter of the nozzle orifice.<sup>100</sup> For an atomic gas  $\gamma = 5/3$ ,  $A = 3.26$  and  $B = 0.075$ , whereas for a diatomic gas  $\gamma = 7/5$ ,  $A = 3.65$  and  $B = 0.40$ . For atomic gases at large distances from the nozzle (*i.e.*  $z/d \gg 1$ ), the Mach number can be approximated by

$$M(z) \approx A (z/d)^{\gamma-1} = 3.26(z/d)^{2/3}. \quad (7)$$

From a thermodynamical treatment of the continuous, adiabatic expansion process, the local temperature  $T(z)$  of the expanding gas can be expressed as

$$T(z) = T_0 \left( 1 + \frac{\gamma-1}{2} M(z)^2 \right)^{-1}, \quad (8)$$

the stream velocity  $v_s(z)$  as

$$v_s(z) = M(z) \sqrt{\frac{\gamma k T(z)}{m}}, \quad (9)$$

and the on-axis density  $n_{||}(z)$  as

$$n_{||}(z) = n_0 \left( 1 + \frac{\gamma-1}{2} M(z)^2 \right)^{-1/(\gamma-1)}, \quad (10)$$

with  $n_0$  the density corresponding to the reservoir stagnation pressure  $p_0$ . At the nozzle orifice, where the gas flow diameter is most restricted by transverse confinement, the Mach number is one. For an atomic gas at large distances from the nozzle, where  $M(z) \gg 1$ , eqn (10) can be approximated by

$$n_{||}(z) \approx 0.150 n_0 (z/d)^{-2}, \quad (11)$$

which scales as the on-axis density of a beam emanating from a point source. When the density of the expanding gas has decreased, the cooling stops and a terminal Mach number  $M_t$  is reached. For rare gases other than helium, the terminal Mach number is given by<sup>101</sup>

$$M_t = 133 \left( \frac{p_0 d}{\text{atm cm}} \right)^{2/5}. \quad (12)$$

For typical experimental parameters ( $d = 0.25$  mm,  $p_0 = 5$  bar), according to eqn (6), the terminal Mach number  $M_t = 58$  is reached at a distance of 19 mm from the nozzle. When the



terminal Mach number is much larger than one, eqn (8) can be approximated to obtain the terminal temperature,

$$T_t = \frac{2T_0}{\gamma - 1} M_t^{-2}. \quad (13)$$

In most deceleration experiments, a heavy rare gas is used as a carrier gas, and the atoms or molecules of interest are added in a smaller concentration (typically <10%) as a seed gas. The expansion is then dominated by the properties of the rare gas, leading to more efficient internal cooling and denser samples of the molecules of interest.

In the expansion region at the exit of the valve, it is possible to produce species which cannot be directly prepared and mixed in a reservoir with the carrier gas. These include reactive species, which must be produced from a precursor molecule by laser photolysis, pyrolysis, laser ablation or electrical discharge. Examples of such species used in deceleration experiments are H (D) atoms produced by photolysis of  $\text{NH}_3$  ( $\text{ND}_3$ ),<sup>59,64,91,102</sup> OH radicals produced by laser photolysis of  $\text{HNO}_3$ ,<sup>74,103</sup> or in an electrical discharge,<sup>104</sup> and NH radicals produced by photolysis of  $\text{HN}_3$ .<sup>79</sup> It is also possible to prepare atoms and molecules in excited metastable states which have more favorable properties for deceleration. This can be achieved by laser excitation, as in the case of CO (single photon excitation at 206 nm to the  $a^3\Pi$  state, which is well suited to Stark deceleration because of its large, mainly linear Stark effect),<sup>56</sup> or in an electrical discharge, which has been used to produce Ne atoms in the  $^3P_2$  state for Zeeman deceleration.<sup>60,105</sup>

At distances on the order of 10 mm downstream from the nozzle orifice, the density and thereby the collision rate in a supersonic beam have dropped such that no further cooling occurs and the temperature of the beam becomes constant. A skimmer is placed in this region to geometrically select only the central part of the beam with the lowest transverse velocities. The skimmer also allows differential pumping of the source chamber (typical pressure  $\approx 10^{-4}$ – $10^{-5}$  mbar) and the deceleration chamber (typical pressure  $\leq 10^{-6}$  mbar). The lower pressure in the deceleration chamber is necessary to prevent losses of the decelerated atoms or molecules by collisions with the background gas, as discussed in more detail in Section 3. Having passed the skimmer, the supersonic beam enters the decelerator. The distance between the nozzle, the skimmer, and the decelerator entrance as well as the size of the skimmer should ideally be matched to the transverse velocity acceptance of the decelerator. A focusing element, such as a hexapole lens, is often inserted between the skimmer and the entrance of the decelerator.<sup>56</sup> As the beam propagates from the nozzle to the entrance of the decelerator, the on-axis density is reduced by the transverse spreading of the beam as described by eqn (11). In a pulsed expansion, velocity dispersion also causes longitudinal spreading of the gas pulse. The magnitude of this effect can be estimated by considering a packet of particles of mass  $m = 20$  amu propagating with a velocity  $v = 300 \text{ m s}^{-1}$  and temperature  $T = 100 \text{ mK}$  and thus a velocity spread  $\sigma_v = \sqrt{kT/m} = 6.4 \text{ m s}^{-1}$ . If the opening function of the valve is approximated by a rectangular pulse with a width of  $\tau = 20 \mu\text{s}$ , the initial longitudinal extent of the gas pulse is 6 mm. After a propagation distance of 20 cm, the

longitudinal spatial profile can be accurately reproduced by a Gaussian profile with a full width at half maximum of 11 mm. When compared to a pulse propagating without velocity dispersion, the peak intensity is thus reduced by a factor of about two (see also Section 3).

## 2.2 Multistage Stark and Zeeman deceleration

In general, the complete deceleration of ground-state polar molecules or paramagnetic atoms and molecules necessitates many successive deceleration steps and the use of long arrays of deceleration stages. In a Stark decelerator these stages consist of pairs of parallel, metallic electrodes in a dipolar configuration while in Zeeman deceleration they are individual solenoids (see Fig. 1). High densities of decelerated particles can only be reached by operating the decelerators in a phase-stable manner, both in the longitudinal and transverse dimensions as first demonstrated by Bethlem *et al.*<sup>56</sup> in the case of multistage Stark deceleration.

Although multistage Stark and Zeeman decelerators have common underlying operating principles, differences in their mode of operation exist beyond the simple replacement of high-voltage electrodes by solenoids. The deceleration stages of multistage decelerators must fulfill several requirements: they must reduce the kinetic energy of the particles; they must keep the packets of particles together in the longitudinal dimension and counteract the effect of velocity dispersion. Finally, they must prevent the spreading of the beam in the transverse dimensions. How these requirements are met is outlined below, following the general formalism introduced by Bethlem and Meijer,<sup>57,106</sup> but with a focus on multistage Zeeman deceleration. We first consider a single particle moving on the axis of the decelerator, and then extend the treatment to a packet of particles, which requires the introduction of the concept of phase stability. Finally, the motion in the transverse dimensions is discussed.

In Fig. 3, schematic views of multistage Stark and Zeeman decelerators are presented. To reduce the kinetic energy of a selected low-field-seeking particle (called the synchronous particle hereafter) propagating along the axis of the decelerator, time-dependent high-field barriers are created as illustrated in Fig. 3b. In the case of a Stark decelerator, this is achieved by applying high electric potentials of opposite polarity to two adjacent electrodes placed in a plane perpendicular to the propagation direction, while in a Zeeman decelerator the potential barrier is created by pulsing a current through a solenoid. As it moves toward the top of this barrier, the low-field-seeking particle gains internal energy, thus losing kinetic energy. By rapidly switching off the fields, this loss of kinetic energy is made irreversible. The amount of kinetic energy  $\Delta E_{\text{kin}}$  that is removed in one deceleration stage depends on the position of the particle when the decelerating field is switched off, as indicated in Fig. 3c.

In this simplified description, the fields are assumed to instantaneously return to zero at the switch-off time. As in the description of the dynamics in charged-particle accelerators,<sup>107,108</sup> a reduced position  $\theta$  is used to describe the longitudinal position of a particle in the decelerator.<sup>71,109</sup> In a Stark decelerator, the successive deceleration stages are separated by a distance  $L$ .

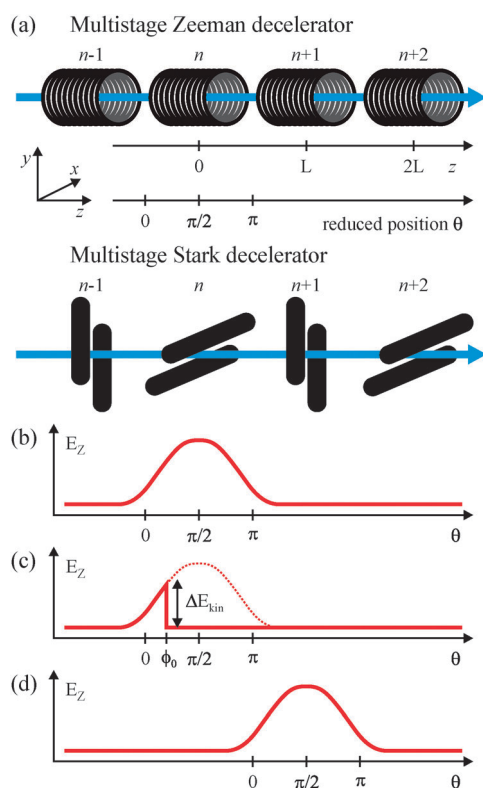


**Fig. 3** Operation principle of multistage Zeeman and Stark decelerators. (a) Definition of the reduced position  $\theta$  with respect to the active stage  $n$ . (b) The potential energy  $E_Z$  of a low-field-seeking particle in stage  $n$ . (c) Definition of the phase angle  $\phi_0$  corresponding to the reduced position reached at the switch-off time of the active stage, and illustration of kinetic energy loss  $\Delta E_{\text{kin}}$ . (d) Potential energy  $E_Z$  of a low-field-seeking particle in stage  $n + 1$ . In (b)–(d), the single-peaked potential of multistage Zeeman decelerators is shown.

Because all electrode pairs pointing in the same direction ( $x$  or  $y$  in Fig. 3a) are electrically connected to each other, the Stark potential  $E_S(z)$  generated along the propagation direction of the beam has a periodicity of  $2L$ ,  $E_S(z) = E_S(z + 2L)$ . The reduced position  $\theta$  is defined so as to reproduce this periodicity ( $\Delta z = 2L \Leftrightarrow \Delta\theta = 2\pi$ ), as illustrated in the figure. In our current generation of Zeeman decelerators, current is pulsed through one coil at a time.<sup>86,87,110</sup> Therefore, the potential generated is single-peaked. A reduced position can nevertheless be defined (see Fig. 3) in analogy with the Stark decelerator. A reduced position  $\theta = 0$  corresponds to the position halfway between deceleration stages  $n - 1$  and  $n$ , and  $\theta = \pi/2$  to the center of the active deceleration stage  $n$ , with two adjacent deceleration stages separated by a distance  $L$  corresponding to the spatial periodicity of the Zeeman decelerator and a reduced distance  $\pi$ .

In its simplest mode of operation, a multistage decelerator is operated such that the kinetic energy is reduced by the same amount in each deceleration stage. This amount depends on the position of the particle when the decelerating field is switched off, as indicated in Fig. 3c. The reduced position which the synchronous particle has reached at the time of switch off is known as the phase angle  $\phi_0$ . Operating the decelerator at high phase angles increases the amount of kinetic energy removed per deceleration stage, with a maximum reached for  $\phi_0 = \pi/2$ . After switching off the field

of deceleration stage  $n$ , the field of deceleration stage  $n + 1$  is switched on, and the deceleration process is repeated. In practice, a small quantization field must be maintained so that the particle does not lose its quantization axis and change state before the deceleration process is repeated in the next stage.<sup>86</sup>

The deceleration sequence of pulses applied to the successive deceleration stages is first calculated and optimized for the synchronous particle. However, dense decelerated samples can only be obtained if an ensemble of particles with phase-space characteristics distributed around that of the synchronous particle are also decelerated to the same final velocity. This is achieved by operating the decelerator in a phase-stable mode,<sup>57,109</sup> which ensures that the decelerated packet has the same phase-space density at the entrance and exit of the decelerator.

In a one-dimensional model, the phase-stable operation results in an oscillatory motion of the particles within a certain phase-stable region about the synchronous particle. In the Zeeman decelerator, the kinetic energy loss  $\Delta E_{\text{kin}}(\phi_0)$  per deceleration stage is given by

$$\Delta E_{\text{kin}}(\phi_0) = E_Z(\phi_0) - E_Z(\phi_0 - \pi) \approx E_Z(\phi_0), \quad (14)$$

where  $E_Z(\phi_0)$  is the Zeeman energy of the particle in the decelerating field, and the field outside the solenoid for  $\theta = \phi_0 - \pi < 0$  is assumed to be zero. The average force acting on the particle over a deceleration stage of length  $L$  is  $\bar{f}(\phi_0) = -E_Z(\phi_0)/L$ . A particle with a small displacement  $\Delta\phi(t) = \phi(t) - \phi_0$  and velocity difference  $\Delta v(t) = v(t) - v_0$  with respect to the synchronous particle experiences an average force

$$\bar{f}(\phi_0 + \Delta\phi) = -E_Z(\phi_0 + \Delta\phi)/L \quad (15)$$

such that its motion relative to the synchronous particle can be described by

$$\frac{mL}{\pi} \frac{d^2\Delta\phi}{dt^2} + \frac{1}{L} [E(\phi_0 + \Delta\phi) - E(\phi_0)] = 0. \quad (16)$$

The phase angle at which the decelerator is operated therefore determines both the amount of kinetic energy that is removed per deceleration stage and the size of the stable phase-space volume. A compromise must therefore be found between maximal energy removal per deceleration stage, which is achieved at large phase angles, and maximal phase-space acceptance at small phase angles.

If effects of the finite rise- and fall-times of the fields and of the transverse motion are also taken into account, it is found from particle trajectory simulations that a multistage Zeeman decelerator is operated most efficiently at phase angles between  $30^\circ$  and  $50^\circ$ , in agreement with experimental observations.<sup>109</sup> Switching times of 10–100 ns are effectively instantaneous for the particle velocities relevant to a deceleration experiment, as the particles do not move significantly within this time interval. These switching times are routinely achievable for the high electrical potentials used in multistage Stark deceleration. However, fast switching of high currents to produce large magnetic fields is more challenging. In the experiments in our laboratory, currents of up to 300 A are pulsed through decelerator solenoids with a minimum-to-maximum rise- and

fall-time of the 2.2 T magnetic field of  $\sim 8 \mu\text{s}$ . The solenoids used are composed of 64 windings of 400  $\mu\text{m}$  diameter copper wire, wound in 4 layers. The inner layer is wound around a quartz tube of 7 mm diameter and each solenoid is 7.3 mm long. Materials with high magnetic permeability can be used to surround each solenoid and constrain the magnetic field lines to increase the maximal field strengths that can be achieved (see, for example, Narevicius *et al.*).<sup>89</sup> While allowing for larger decelerating forces and a smaller number of deceleration stages, the temporal behavior of the magnetic fields is more complex, making the calculation of pulse sequences and particle-trajectory simulations more complicated than for solenoids surrounded by non-magnetic materials.

The finite rise and fall times of the magnetic deceleration fields of a Zeeman decelerator cause some ambiguity in the definition of the phase angle and necessitate that a distinction be made between the nominal phase angle and the effective phase angle (see Wiederkehr *et al.*<sup>109</sup> for more details). The nominal phase angle  $\phi_0$  is defined as the reduced position reached by the synchronous particle when the switch-off of the field is initiated. The finite switch-off times in a multistage Zeeman decelerator increase the effective phase angle with respect to this nominal phase angle. The consequence of this increase in effective phase angle is that the decelerating particles continue to experience longitudinal and transverse magnetic field gradients as the coil is being switched off, with the result that the phase-space acceptance is modified with respect to the acceptance under conditions with instantaneous switching.<sup>109</sup>

Further differences between Stark and Zeeman decelerators become apparent when considering the transverse dynamics. The different symmetries of the two types of decelerator are of particular importance when considering how the deceleration stages prevent the beam from spreading out in the transverse dimensions. In a Stark decelerator, the deceleration stages are sequentially oriented along the  $x$  and  $y$  dimensions, perpendicular to the direction of propagation of the molecular beam (see Fig. 3a). The electric fields of electrode pairs  $n$ ,  $n + 2$ , ... focus the beam in the vertical ( $y$ ) direction, whereas the fields of electrode pairs  $n - 1$ ,  $n + 1$ , ... focus the beam in the horizontal ( $x$ ) direction (see van de Meerakker *et al.*).<sup>111</sup> The cylindrical symmetry of the solenoids in a Zeeman decelerator implies that the beam is focussed simultaneously in the  $x$  and  $y$  dimensions. Moreover, the radial dependence of the decelerating magnetic fields exhibits some important characteristics. In the center of the active coil (at  $\theta = \pi/2$ ), the magnetic field has a saddle point and exerts a transverse focusing force. As one moves back (towards smaller  $\theta$ ), the transverse focusing becomes weaker, and the radial field profile changes from concave to convex. In this region, the field is transversely defocusing.

In their work on Stark deceleration a range of approaches to the design of multistage decelerators have been investigated by Meijer and co-workers. By applying suitable waveforms to microstructured electrodes deposited on a glass substrate, a supersonic beam of CO molecules was decelerated and trapped on a chip.<sup>15,112</sup> In this chip decelerator the molecules remain trapped in an electric field minimum during the whole deceleration process, enabling higher efficiencies and smaller losses.

However, the small dimensions of the traps limit the number of particles accepted in a single trap minimum. The trapping field confines the particles only in the propagation direction and the direction perpendicular to the substrate, but the particles are not confined in the third dimension. A similar method has been adopted and scaled up to the dimensions of a conventional multistage decelerator by using macroscopic ring electrodes, which allows for three-dimensional confinement of the decelerated molecules in the moving traps.<sup>69</sup> Compared to a conventional Stark decelerator, such a moving-trap ring decelerator offers the advantage of an increased phase-space acceptance. Recently, guiding<sup>88</sup> and deceleration<sup>113</sup> of metastable atoms in moving magnetic traps has also been demonstrated. These deceleration experiments rely on the same principle of a moving trap minimum as previously exploited in Rydberg–Stark deceleration<sup>90</sup> (see also Section 2.3).

### 2.3 Rydberg–Stark deceleration

In contrast to the multistage deceleration techniques described above, Rydberg–Stark deceleration of atoms and molecules in pulsed supersonic beams does not rely on the existence of a ground-state electric or magnetic dipole moment. Instead, the samples to be decelerated are photoexcited to Rydberg states of high principal quantum number  $n$ , which exhibit large electric dipole moments. The electric dipole moments of high Rydberg states scale with  $n^2$ , and, at  $n = 30$ , take values up to  $3/2n^2ea_0 \text{ Cm} \equiv 3400 \text{ Debye}$ .<sup>114</sup> As all atoms and molecules possess Rydberg states, this approach is quite general and therefore applicable to species that cannot be decelerated by multistage Stark or Zeeman deceleration, including for example  $\text{H}_2$ .

In an external electric field each Rydberg state of the hydrogen atom splits into a manifold of Stark states as depicted in Fig. 2d in the energy range around  $n = 30$ . These states arise from the field-induced mixing of states of different orbital angular momentum,  $\ell$ , and can be labelled by a quantum number  $k$ , which represents the difference between the two parabolic quantum numbers  $n_1$  and  $n_2$  used in the solution of the Schrödinger equation of the H atom in parabolic coordinates,<sup>114</sup>  $k$  takes values from  $-(n - |m_\ell| - 1)$  to  $+(n - |m_\ell| - 1)$  in steps of two. The dipole moment of each state is given by  $|\vec{\mu}_{nk}| = 3/2nkea_0$ . To first order, the Stark shift of each of these states can be expressed in atomic units as

$$E_s = \vec{\mu}_{nk} \cdot \vec{F} = \frac{3}{2}nk|\vec{F}|, \quad (17)$$

where the atomic unit of electric field strength is equal to  $5.4 \times 10^9 \text{ V cm}^{-1}$  and the atomic unit of energy is the Hartree ( $E_H$ ). The outermost states of the manifold labelled  $n = 30$  have the largest values of  $|k|$  and hence the largest electric dipole moments ( $\sim 3400 \text{ Debye}$ ). The states that are shifted toward lower (higher) energies with increasing electric field strength are those with their dipole moments oriented parallel (antiparallel) to the external electric field vector and have negative (positive) values of  $k$ .

A schematic diagram of an electrode configuration used for Rydberg–Stark deceleration and electrostatic trapping is presented in Fig. 1c.<sup>93</sup> Because of the large electric dipole moments of the states employed in these experiments, supersonic beams of light species such as H and  $\text{H}_2$  can be

decelerated from speeds of  $\sim 500 \text{ m s}^{-1}$  to zero velocity in the laboratory frame within distances of only a few millimetres and on time scales on the order of  $10 \mu\text{s}$ . To achieve maximum efficiency in the deceleration of atoms or molecules in Rydberg states, the states involved should ideally (i) be hydrogenic, in that they have quantum defects near zero and therefore a predominantly linear Stark shift, and (ii) have sufficiently long lifetimes that they can be decelerated before they decay. These criteria are both met in atomic hydrogen for Rydberg states prepared by resonant two-photon excitation from the ground state. The fluorescence lifetime of a Rydberg state of atomic hydrogen with  $n = 30$  in the presence of an electric field is  $\sim 220 \mu\text{s}$ . However, meeting these requirements in other species necessitates additional measures.

The non-hydrogenic character of a manifold of Rydberg–Stark states arises from the presence of core penetrating, low- $\ell$  Rydberg states with non-zero quantum defects. At zero electric field, these states are not degenerate with the high- $\ell$  states and exhibit a quadratic Stark effect when the field strength is increased. At the field where the manifold of Stark states associated with one  $n$  crosses that of the next  $n$ , the presence of the low- $\ell$  states in the Stark manifold gives rise to avoided crossings. The electric field at which the first crossing occurs is known as the Inglis–Teller field,  $F_{\text{I.T.}} = 1/3n^5$  in atomic units. At an avoided crossing of this kind, a state with a dipole moment oriented in one direction can be converted into one of the opposite orientation, making it difficult to control the force exerted on an atom or molecule and limiting the useable electric fields for deceleration to those below  $F_{\text{I.T.}}$ .

The lifetimes of atomic Rydberg states that lie below the first ionization limit are governed by the rate of spontaneous emission toward the ground state. This rate depends primarily on the overlap between the Rydberg-state wavefunction and the wavefunction of the ground state, and, in the absence of an external field, scales as  $n^{-3}$ . An external electric field mixes states of different orbital angular momentum, leading to an increase in the lifetime of the low-angular-momentum states, which are generally accessible by laser excitation from the ground state. In molecular Rydberg states an additional decay mechanism, known as predissociation, can occur below the first ionization limit. This process involves the transfer of energy from the Rydberg electron to the nuclear degrees of freedom of the molecule. Predissociation is generally a much more rapid process than spontaneous emission, and occurs predominantly for core-penetrating, low- $\ell$  Rydberg states.

Because non-hydrogenic behavior in an electric field and short lifetimes arising from predissociation both result from the presence of low- $\ell$  Rydberg states in a Stark manifold, these problems can be circumvented simultaneously through the preparation of states which do not exhibit any low- $\ell$  character. This is achieved by photoexcitation of states with a well defined azimuthal quantum number,  $|m_\ell|$ , such that states with values of  $\ell < |m_\ell|$  are not contained in the Stark manifold. In the case of Rydberg–Stark deceleration of  $\text{H}_2$ , a resonant three-photon excitation scheme, using circularly polarized light, was employed to prepare non-penetrating  $|M_J| = 3$  states in the range  $n = 20\text{--}40$  of the Rydberg series converging to the lowest ionization limit for which  $N^+ = 0$ .<sup>94,115</sup>

Following early proposals by Breeden and Metcalf<sup>116</sup> and Wing,<sup>117</sup> first experiments exploiting the interaction of samples in Rydberg states with inhomogeneous electric fields involved the deflection of a pulsed supersonic beam of krypton atoms by the time-independent dipolar electric field distribution surrounding a pair of cylindrical electrodes.<sup>118</sup> These experiments were carried out by Softley and co-workers at the University of Oxford and led to a proof-of-principle demonstration of the deceleration of a fast beam of hydrogen molecules.<sup>61,119</sup> Experiments were then carried out at ETH Zurich with pulsed supersonic beams of argon atoms. These experiments were first performed in the static field of a pair of electrodes in a wedge configuration, generating an electric field gradient along the axis of the atomic beam, and highlighted the effects of non-hydrogenic states on the deceleration process close to the Inglis–Teller limit.<sup>62</sup>

By introducing time-dependent electric fields the efficiency of the deceleration process could be improved, particularly in non-hydrogenic species.<sup>90</sup> In this way large electric field gradients could be generated at the position of the accelerating or decelerating bunch of Rydberg atoms while ensuring that the field strength at this position was kept below the Inglis–Teller field where the influence of non-hydrogenic states is most significant. By applying potentials with an exponentially decaying time dependence to a set of four electrodes in a quadrupole configuration, the initial kinetic energy of a beam of argon atoms could be changed by up to  $E_{\text{kin}}/hc \sim \pm 60 \text{ cm}^{-1}$ . This change in kinetic energy is 2.7 times the Stark energy in the maximal field experienced by the atoms during deceleration/acceleration. Using time-dependent fields, one can ensure that non-hydrogenic samples do not experience fields larger than the Inglis–Teller field during deceleration or that samples of hydrogen atoms or high- $|M_J|$  hydrogenic states of other species do not experience a field of sufficient strength to result in ionization. This work also opened up the possibility to efficiently decelerate<sup>90</sup> and transversely focus beams of argon atoms,<sup>120</sup> reflect beams of Rydberg hydrogen atoms using a Rydberg atom mirror,<sup>64</sup> and later to efficiently load Rydberg atoms and molecules into electrostatic traps.<sup>92–94,115</sup>

The Rydberg–Stark deceleration and trapping experiments that have so far been performed to trap atomic and molecular hydrogen have only required the use of single-stage decelerators. The design used, and presented in Fig. 1c, acts simultaneously as a single-stage decelerator and three-dimensional electrostatic trap. The four electrodes located above and below the molecular beam in this figure are operated in a quadrupole configuration, typically at potentials of  $\pm 20 \text{ V}$ . This provides a sufficiently strong and homogeneous field at the position of photoexcitation, where the laser beams cross the molecular beam, to permit the preparation of selected Stark states for deceleration. It also forms a quadrupole field distribution with a minimum located at the center of the four electrodes which is suitable for trapping samples in low-field-seeking Stark states. Two endcap electrodes close off the trap in the third dimension and can be operated at potentials of opposite sign to create a non-zero field at the minimum of the trap.<sup>93</sup> This design is therefore an electrostatic trap with a non-zero electric field minimum and is the electric analogue of the Ioffe–Pritchard magnetic trap.<sup>121,122</sup>



After photoexcitation to selected low-field-seeking Rydberg–Stark states, high potentials of between 1 kV and 4 kV are applied to the pair of electrodes furthest from the skimmer to generate a positive electric field gradient in the direction of propagation of the atomic or molecular beam at the position of the excited atoms or molecules. To efficiently load the electrostatic trap, these high potentials then decay exponentially with an adjustable time constant of  $\sim 2 \mu\text{s}$  back to the initial quadrupole configuration. This approach has the advantages that (i) using time-dependent electric fields maximal deceleration can be achieved within a given distance while limiting the field experienced by the decelerating particles, and (ii) because the particles are always confined in a continuously moving electric field minimum as they are decelerated, particle loss, particularly at low longitudinal velocities, is almost negligible. Detection of the trapped ensemble is achieved by pulsed electric-field ionization and extraction of the resulting ions toward a micro-channel plate detector upon application of high positive potentials to the pair of electrodes located closest to the skimmer in Fig. 1c. This electrode configuration has been employed to decelerate and trap hydrogen atoms and molecules in Rydberg states around  $n = 30$ .<sup>93,94</sup> The deceleration concept utilizes the same principle of a continuously moving trap minimum as that which has been exploited in recent Stark and Zeeman deceleration experiments mentioned at the end of Section 2.2.

Presented in Fig. 4 are three spectra in which the wavenumber of a laser employed in the photoexcitation of Rydberg states of  $\text{H}_2$  was scanned in the vicinity of the transition to the  $n = 22$  level of the Rydberg series converging to a  $\text{H}_2^+$  ion core with no rotational angular momentum, *i.e.*  $N^+ = 0$ . The first measurement (Fig. 4a) shows the transition to the field-free 22f,  $|M_J| = 3$  level recorded in zero electric field by pulsed electric field ionization immediately after photoexcitation in a set of electrodes used for Rydberg–Stark deceleration and electrostatic trapping. Potentials were then applied to the trap electrodes in a quadrupole configuration used for trapping to lift the degeneracy of the Stark states which are partially resolved in Fig. 4b. By then switching on the deceleration potentials, loading the trap and measuring after a trapping time of  $50 \mu\text{s}$ , only the outer low-field-seeking Stark states between  $k = +10$  and  $k = +18$  are observed. These states have sufficiently large electric dipole moments to be efficiently decelerated and loaded into the trap. With one set of trapping and deceleration potentials a range of states of different principal quantum number above a certain minimum value can be trapped.<sup>94,115</sup>

The process of deceleration and trap loading using a continuously moving minimum employed in these experiments is extremely efficient. In general the traps that have been developed have been designed so that the phase-space distribution of the initially excited ensemble of Rydberg atoms or molecules matches the shape and depth of the moving field minimum and trap. For the outer Stark states at a principal quantum number of  $n = 30$ , trap depths of up to 3 K can be easily achieved with potentials on the trap electrodes on the order of 10–20 V with the spatial extent of the trapping volume covering a range of a few cubic millimetres. The bunches of excited Rydberg atoms prepared by photoexcitation typically

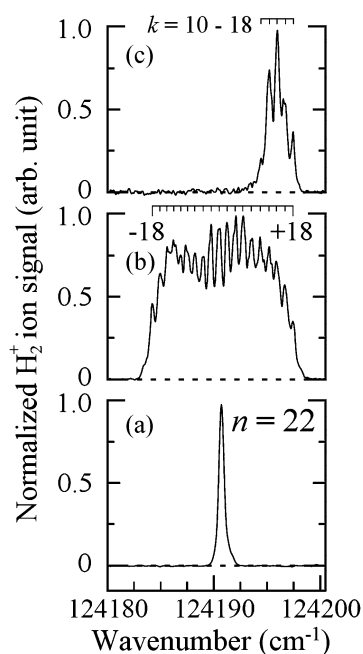


**Fig. 4** State-selective trapping of  $\text{H}_2$ . (a) The zero-field 22f Rydberg state of  $\text{H}_2$ , (b) the  $n = 22$  Stark manifold in an electric field of  $278 \text{ V cm}^{-1}$  and (c) the outer  $k = 10$ – $18$  low-field-seeking Stark states detected after deceleration and electrostatic trapping for  $50 \mu\text{s}$ .<sup>94</sup>

have relative translational temperatures on the order of 100 mK and approximately cylindrical spatial distributions with diameters on the order of 500–800  $\mu\text{m}$ , limited by the size of the coherent beams of vacuum ultraviolet and ultraviolet radiation used for excitation, and lengths of a few millimetres.<sup>93</sup> Loss of particles during deceleration or trapping is dominated by the effects of blackbody radiation and collisions with the undecelerated part of the gas pulse.<sup>63</sup>

### 3 Losses during deceleration

In neutral-particle decelerators, possible loss mechanisms include collisions with the background gas, collisions of the particles which are decelerated with the undecelerated carrier gas beam, and transitions from the state for which the deceleration sequence is optimized to other internal states. These loss mechanisms are discussed in this section.

#### 3.1 Nonadiabatic transitions near zero field and adiabatic transitions at high field

The effect of nonadiabatic transitions in a Stark decelerator has been treated in detail by Wall *et al.*<sup>81</sup> In a Zeeman decelerator, a small quantization field must be maintained at all times by switching on the next deceleration solenoid before the field of the previous solenoid has reached zero.<sup>86</sup> Because of the cylindrical symmetry of the solenoid fields, the problem of alternating directions of the field in the transverse direction as discussed by Wall *et al.* does not occur here.

To investigate the effect of the switching of the fields on the deceleration efficiency in a Zeeman decelerator, measurements have been performed in which the overlap time between the switch-off and switch-on of the current in successive

decelerator solenoids was varied.<sup>86,123</sup> The effects of zero-field periods between successive current pulses applied to adjacent solenoids are illustrated in Fig. 5 in the case of the deceleration of metastable neon atoms. This figure shows the time-of-flight distributions recorded in multistage Zeeman deceleration experiments carried out on a supersonic beam of metastable neon initially moving at a velocity of  $525 \text{ m s}^{-1}$  using a decelerator consisting of 36 solenoids. The top trace was obtained using a pulse sequence in which the active solenoid,  $n$ , was switched off  $10 \mu\text{s}$  after the next solenoid  $n + 1$  was switched on so that the decelerated atoms never experienced a period of time in the absence of a field. The peak in the time-of-flight distribution corresponding to the decelerated atoms (final velocity of  $400 \text{ m s}^{-1}$ ) is observed at  $\sim 2.7 \text{ ms}$ . Reducing the duration of the overlap between successive pulses to zero does not cause any significant change in the time-of-flight profile. Changes in the decelerated-atom peak become observable when the active solenoid is turned off more than  $4 \mu\text{s}$  before the next solenoid is turned on, *i.e.* for  $\Delta t > -4 \mu\text{s}$  (see inset of Fig. 5 for the definition of  $\Delta t$ ). Under these conditions, the fields at the position of the decelerating atoms become small enough that non-adiabatic transitions start to affect the deceleration efficiency. The decelerated-atom signal completely disappears when  $\Delta t > 8 \mu\text{s}$  which corresponds to the time needed for the current driven through the active coil to have decayed to zero.

Particle loss in Zeeman and Stark deceleration can also occur when the decelerated molecules move through regions of space in which the field induces an avoided crossing between different Zeeman or Stark sub-levels. The adiabatic traversals of these crossings that take place as the molecules travel through these regions change their dipole moments which in

most decelerators result in the ejection of the molecules from the decelerated bunch. These effects have been studied experimentally in Rydberg–Stark deceleration<sup>62</sup> and quantified in the recent work on the Rydberg–Stark deceleration and electrostatic trapping of  $\text{H}_2$ .<sup>94,115</sup>

### 3.2 Collisional losses

Both elastic and inelastic collisions can contribute to the total collisional loss. Elastic collisions with the background gas or the carrier gas eject the decelerated particles from the accepted phase-space volume of the decelerator. Inelastic collisions, in addition, induce transitions from the state for which the deceleration sequence is optimized to states less suited for deceleration, which leads to particle loss in the experiment. In general, a cold sample in a single internal state is desired for many applications. Therefore, even if these molecules in other internal states could be decelerated, it is advantageous to minimize their contribution.

While reducing the background pressure in the deceleration vacuum chamber minimizes losses by collisions with the background gas, collisions between the particles to be decelerated and those in the carrier gas pulse are unavoidable. The resulting losses can be estimated using typical values for the collision cross sections, the properties of the carrier gas pulse, and the motion of the particles in the decelerator.

When a packet of particles propagates a distance  $dl$  through a homogeneous gas of density  $n$ , the relative change in intensity is given by

$$\frac{dI}{I} = -\frac{1}{\lambda} dl = -\sigma n dl \quad (18)$$

with  $\lambda = (\sigma n)^{-1}$  the mean free path, and  $\sigma$  the collision cross section. By integrating this differential equation, the transmission  $T$  is obtained

$$T(l) = \frac{I(l)}{I_0} = \exp(-\sigma n l), \quad (19)$$

with  $I_0$  the initial intensity and  $I(l)$  the intensity after a propagation distance  $l$ . These expressions are analogous to the Lambert–Beer law in optics. Expressing the distance  $dl = v(t)dt$  in terms of a time interval  $dt$  and the packet velocity  $v(t)$ , eqn (18) can be rewritten in the form

$$\frac{dI}{I} = -\sigma(v)n(t)v(t)dt, \quad (20)$$

where we explicitly include a velocity dependence of the collision cross section, and a time dependence of the gas density and the velocity of the particle packet.

We now consider a single particle in the decelerated packet. The average time between collisions for a single particle of velocity  $v$  is given by  $t_{\text{coll}} = \lambda/v = (\sigma n v)^{-1}$ . This motivates the definition of the collision rate  $R(t)$  at which a single particle in the packet undergoes collisions with the other particles as

$$R(t) = \sigma(v)n(t)v(t). \quad (21)$$

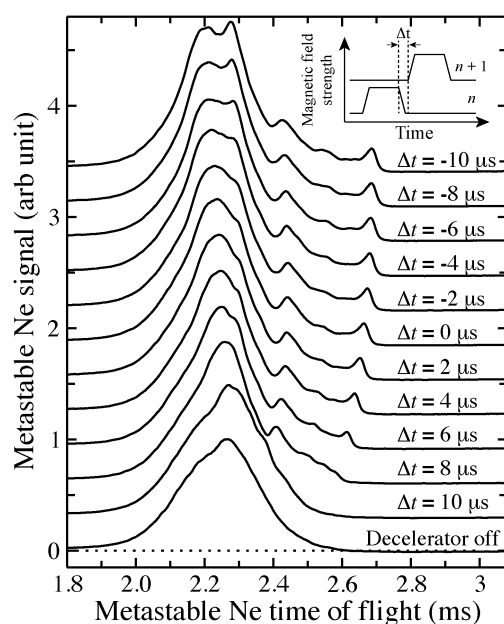


**Fig. 5** Deceleration of metastable  $^3\text{P}_2$  Ne atoms with a 36-stage Zeeman decelerator.<sup>123</sup> The time delay  $\Delta t$  between the initiation of the switch-off and switch-on of the current in solenoids  $n$  and  $n + 1$ , respectively, for each time-of-flight measurement is indicated to the right of each dataset.

By inserting eqn (21) into (20) and integrating, we obtain

$$\ln\left(\frac{I(t)}{I(t_0)}\right) = - \int_{t_0}^t R(t') dt', \quad (22)$$

which can be expressed in terms of the transmission

$$T = \frac{I(t)}{I(t_0)} = \exp\left(- \int_{t_0}^t R(t') dt'\right). \quad (23)$$

A calculation of  $R(t)$  suffices to predict the transmission of the whole packet of particles. If the packet of particles cannot be considered monoenergetic, an average over its velocity distribution must be performed.

**3.2.1 Collisions with the background gas.** We begin by estimating losses by collisions with the background gas. For a single particle in the decelerated packet propagating through a homogeneous background gas of density  $n_{\text{BG}}$ , the collision rate  $R(t)$  is given by

$$R(t) = \sigma(v_{\text{rel}}) n_{\text{BG}} v_{\text{rel}}(t) \quad (24)$$

according to eqn (21). Here,  $v_{\text{rel}}(t)$  is the relative velocity between the colliding particles and  $\sigma(v_{\text{rel}})$  is the collision cross section.

At the beginning of the deceleration process, the velocity of the particles fulfilling the conditions for phase-stable deceleration is equal to the stream velocity. At later times, when the particle packet has been decelerated significantly, the relative velocity is entirely dominated by the thermal velocity distribution of the background gas. To simplify the description, we make the assumption that during the whole deceleration process the relative velocity is given by the mean thermal velocity of the background gas  $v_{\text{rel}} = \sqrt{\frac{8kT_{\text{BG}}}{\pi m_{\text{BG}}}} = 470 \text{ m s}^{-1}$  ( $\text{N}_2$  at room temperature). In addition, we assume that the cross section  $\sigma$  is velocity independent in this thermal collision energy range. With these approximations, the transmission  $T$  of the decelerated packet is

$$T = \exp(-\sigma n_{\text{BG}} v_{\text{rel}} \Delta t), \quad (25)$$

where  $\Delta t$  is the duration of the deceleration process. Values of  $T$  obtained for a range of cross sections  $\sigma$  and background pressures  $p_{\text{BG}}$  for a typical duration of the deceleration process of  $\Delta t = 5 \text{ ms}$  are listed in Table 2. Our calculations show that for a background pressure of  $10^{-6}$ – $10^{-7}$  mbar and values of the collision cross section below  $10^{-14} \text{ cm}^2$  the packet traverses the vacuum chamber without significant loss. These simple considerations highlight the importance of separating the gas source chamber and the decelerator by a skimmer and maintaining efficient differential pumping.

**3.2.2 Collisions with the undecelerated carrier gas pulse.** To investigate the role of collisions with the undecelerated carrier gas pulse, we consider the multistage Zeeman deceleration of oxygen  $\text{O}_2$  seeded in Kr. Typical parameters of the source are a temperature of  $T_0 = 200 \text{ K}$  and a stagnation pressure of  $p_0 = 5 \text{ bar}$ , resulting in a density in the stagnation reservoir of  $n_0 = 1.8 \times 10^{20} \text{ cm}^{-3}$ . The diameter of the nozzle orifice is  $d = 0.25 \text{ mm}$ , and we approximate the nozzle opening

**Table 2** Transmission  $T$  of a decelerated bunch of molecules through a room-temperature background gas for different values of the collision cross section  $\sigma$  and the background pressure  $p_{\text{BG}}$ , assuming a deceleration time of  $\Delta t = 5 \text{ ms}$  and a constant relative velocity of  $v_{\text{rel}} = 470 \text{ m s}^{-1}$

	$p_{\text{BG}}/\text{mbar}$		
$\sigma/\text{cm}^2$	$1 \times 10^{-5}$	$1 \times 10^{-6}$	$1 \times 10^{-7}$
$10^{-13}$	0.003	0.560	0.944
$10^{-14}$	0.560	0.944	0.994
$10^{-15}$	0.944	0.994	0.999

function by a square pulse with a width of  $\tau = 20 \mu\text{s}$ , corresponding to that achievable with valves of Even–Lavie type.<sup>124</sup> With these parameters, the following properties of the supersonic beam of Kr can be calculated using the expressions given in Section 2.1: Terminal Mach number  $M_t = 58$ , terminal stream velocity  $v_t = 313 \text{ m s}^{-1}$ , terminal temperature  $T_t = 0.18 \text{ K}$ .

To obtain the local collision rate  $R(t)$  of a single particle in the decelerated packet with the undecelerated carrier gas pulse as defined by eqn (21), we restrict our treatment to the symmetry axis  $z$  of the Zeeman decelerator. The decelerator entrance is located at a position  $0.2 \text{ m}$  from the nozzle. In the Zeeman decelerator, the distance between adjacent deceleration solenoids is  $\Delta z = 11 \text{ mm}$ .<sup>87,109</sup> At a phase angle of  $\phi_0 = 45^\circ$ , the energy loss of the synchronous  $\text{O}_2$  molecule in the  $^3\Sigma_g^-$  ( $N = 1$ ,  $J = 2$ ,  $M_J = 2$ ) state (see Fig. 2) is  $\Delta E_Z/(hc) = 1.5 \text{ cm}^{-1}$  per deceleration stage. This can be described by a constant force  $F = -\frac{\Delta E_Z}{\Delta z}$  or a constant deceleration  $a = -m_{\text{O}_2}^{-1} \frac{\Delta E_Z}{\Delta z}$  acting on the synchronous molecule.

The local collision rate of a particle in the decelerated packet with the carrier gas pulse is

$$R(z, t) = \sigma(\Delta v(t)) n(t) \Delta v(t) \quad (26)$$

where  $z = z_{\text{decel}}(t)$  is the position of the decelerated packet,  $\sigma(\Delta v(t))$  is the collision cross section,  $n(t)$  is the density of the carrier gas pulse at the position of the decelerated particle, and  $\Delta v(t)$  is the relative velocity between the carrier gas and the decelerated particle. We neglect collisions with other particles in the decelerated packet; this is justified by the lower density of the decelerated packet, typically  $< 10^{10} \text{ cm}^{-3}$ , compared to the density of  $\sim 10^{13} \text{ cm}^{-3}$  of the carrier gas at the decelerator entrance.

To describe the spatial distribution of the carrier gas pulse at time  $t > 0$  ( $t = 0$  corresponds to the middle of the nozzle opening function), we approximate its longitudinal velocity distribution by

$$f(v_z) dv_z = \frac{1}{\sqrt{2\pi}\sigma_v} \exp\left(-\frac{(v_z - v_t)^2}{2\sigma_v^2}\right) dv_z, \quad (27)$$

and the normalized spatial distribution at time  $t > 0$  by

$$\tilde{S}(z, t) dz = f\left(\frac{z}{t}\right) t^{-1} dz. \quad (28)$$

The initial longitudinal spatial distribution function resulting from the finite nozzle opening time  $\tau$  is described by

$$g(z) = \begin{cases} (v_t \tau)^{-1} & \text{for } -v_t \tau/2 \leq z \leq v_t \tau/2, \\ 0 & \text{otherwise.} \end{cases} \quad (29)$$

The normalized spatial distribution of the undecelerated carrier gas pulse at a time  $t > 0$  is then obtained from a convolution of these distributions

$$\tilde{S}_1(z, t) dz = \left[ \int_{-\infty}^{+\infty} f\left(\frac{z-z'}{t}\right) t^{-1} g(z') dz' \right] dz. \quad (30)$$

Note that  $\tilde{S}(z, t)$  and  $\tilde{S}_1(z, t)$  are normalized such that  $\int_{-\infty}^{+\infty} \tilde{S}(z, t) dz = \int_{-\infty}^{+\infty} \tilde{S}_1(z, t) dz = 1$ . When the packet has reached the decelerator entrance, the spatial spread caused by the velocity dispersion dominates over the spatial spread resulting from the finite opening time of the valve, and  $\tilde{S}_1(z, t)$  is well approximated by  $\tilde{S}(z, t)$ .

In a continuous expansion, the on-axis density  $n_{\parallel, \text{cw}}(z, t)$  is given by eqn (11). In a pulsed expansion with velocity dispersion, this expression cannot be used to predict the peak density, because the peak density decreases with increasing propagation time. This decrease can be accounted for by introducing a new spatial distribution function  $S_1(z, t)$ , which is normalized such that its peak value is one for  $t \rightarrow 0$  (for  $t = 0$  the function is not defined):

$$S_1(z, t) = g(0)^{-1} \tilde{S}_1(z, t). \quad (31)$$

The density profile  $n_{\text{Kr}}(z, t)$  of the carrier gas pulse, shown in Fig. 6, is then given by

$$n_{\text{Kr}}(z, t) = n_{\parallel, \text{cw}}(v_t t) S_1(z, t). \quad (32)$$

In the decelerator,  $\tilde{S}_1(z, t)$  is well approximated by  $\tilde{S}(z, t)$ , so that the distribution function

$$S(z, t) = g(0)^{-1} \tilde{S}(z, t) \quad (33)$$

can be used.

The difference in position between the carrier gas pulse and the synchronous particle propagating through the decelerator is shown in Fig. 7a. The density profile of the carrier gas pulse  $n_{\text{Kr}}(z, t)$  on the axis of the decelerator at time  $t$  is given by eqn (32) and displayed in Fig. 6. The local density of the carrier gas pulse overlapping with the decelerated packet is determined using

$$n(t) = \int_{-\infty}^{+\infty} n_{\text{Kr}}(z, t) h(z, t) dz, \quad (34)$$

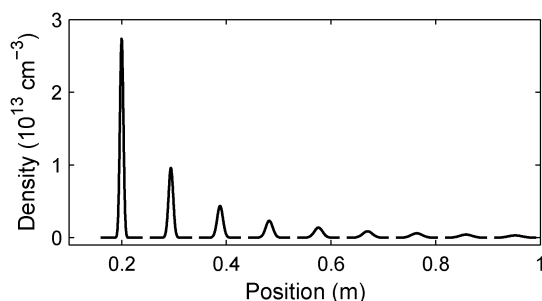


**Fig. 6** The on-axis density profile  $n_{\text{Kr}}(z, t)$  of the carrier gas pulse propagating through the decelerator. The center of the gas pulse reaches the decelerator entrance, located at 0.2 m, at  $t_0 = 0.64$  ms. Thereafter, the density profile is plotted every 0.3 ms.

where  $n_{\text{Kr}}(z, t)$  is defined in eqn (32) with  $h(z, t) = (\sqrt{2\pi}\sigma_z)^{-1} \exp(-\frac{(z-z_{\text{decel}}(t))^2}{2\sigma_z^2})$ ,  $\sigma_z = 1$  mm describing the spatial spread of the decelerated packet. We see from Fig. 7b that the local density  $n(t)$  decreases as the packet of decelerated particles propagates through the decelerator.

At the beginning of the deceleration process, the particles in the decelerated packet are embedded in the carrier gas pulse, which propagates with the same velocity. Therefore, the relative velocity in a collision is given by the mean relative velocity of the carrier gas  $\langle v \rangle = \sqrt{\frac{8kT_{\text{L}}}{\pi m_{\text{Kr}}}}$ . Because the velocity spread of the phase-stable particles is much smaller than the velocity spread of the carrier gas, the latter gives the dominant contribution to the collision energy at early times. At later times, when the particle packet has been decelerated substantially, the relative velocity is dominated by the velocity difference  $v_{\text{decel}}(t) - v_t$  between the terminal velocity of the supersonic

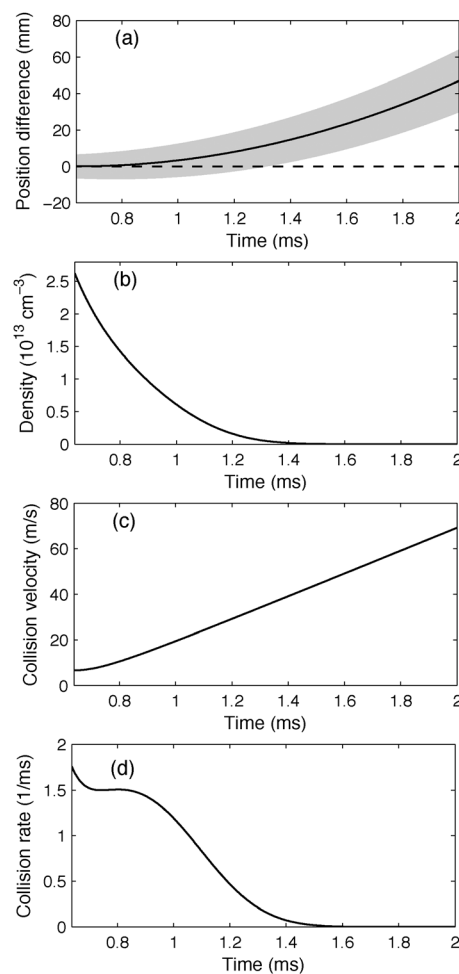


**Fig. 7** (a) The displacement,  $z_{\text{carrier}}(t) - z_{\text{decel}}(t)$ , of the synchronous particle from the centre of the carrier gas pulse propagating through the decelerator. The shaded region indicates the range within which 95% of the carrier gas pulse density is found. The horizontal line indicates the position of the synchronous particle. (b) The local density  $n(t)$  of the carrier gas pulse at the position of the synchronous particle. (c) The average relative velocity between the synchronous particle and a Kr atom in the carrier gas pulse. (d) The collision rate of the synchronous particle with the carrier gas pulse.



beam and the velocity of the decelerated packet. To link these two limiting situations, we use the function

$$\Delta v(t) = \sqrt{(v_{\text{decel}}(t) - v_t)^2 + \frac{8kT_t}{\pi m_{\text{Kr}}}}, \quad (35)$$

displayed in Fig. 7c.

Since no experimental data are available for the relevant range of collision velocities, we assume the total scattering cross section  $\sigma$  to be velocity independent. The value  $\sigma = 10^{-13} \text{ cm}^2$  is estimated from measurements in the range  $v = 500\text{--}1000 \text{ m s}^{-1}$  by Aquilanti *et al.*,<sup>125,126</sup> which are scaled to a collision velocity in the range  $10\text{--}100 \text{ m s}^{-1}$  by noting that  $\sigma(v)v^{2/5} = Q(C_6)$  is on average constant for particles interacting through a long-range  $C_6/R^6$  potential.<sup>127,128</sup> At the beginning of the deceleration process, the collision energy is determined by the energy spread of the supersonic beam and corresponds to a temperature of  $\approx 100 \text{ mK}$ . The true cross section may show variations because of resonances and thresholds for internal excitation.

Based on the assumption of a velocity-independent collision cross section, the collision rate is given by  $R(t) = \sigma n(t)\Delta v(t)$ .  $R(t)$ , shown in Fig. 7d, is proportional to the product of the density and collision-velocity curves depicted in Fig. 7b and Fig. 7c, and shows a complex behavior: As the carrier gas pulse propagates along the decelerator its density decreases. The local density at the position of the decelerated packet also decreases as the decelerated packet moves out of the carrier-gas pulse. The increase in collision velocity, however, partially compensates the decrease in local density of the carrier gas pulse and gives rise to the shoulder appearing in  $R(t)$  at  $\sim 0.8 \text{ ms}$  (see Fig. 7d). The value of the initial collision rate of around  $1.7 \text{ ms}^{-1}$  during the first  $\sim 0.8 \text{ ms}$  indicates that collisional loss with the carrier gas are significant. However, after  $1 \text{ ms}$  of deceleration, the decelerated packet has moved out of the gas pulse and losses become negligible.

The packet of decelerated molecules enters the decelerator at  $t_1 = 0.64 \text{ ms}$  and reaches the end of the decelerator ( $v_{\text{decel}} = 0 \text{ m s}^{-1}$ ) at  $t_2 = 6.8 \text{ ms}$ . The transmission estimated with our model is

$$T = \frac{I(t_2)}{I(t_1)} = \exp\left(-\int_{t_1}^{t_2} R(z, t) dt\right) = 0.5. \quad (36)$$

These considerations indicate that collisions with the carrier gas can be significant in multistage deceleration, but the numbers in our model are sensitive to the source parameters. For example, reducing the stagnation pressure from  $5 \text{ bar}$  to  $2 \text{ bar}$  increases the transmission to  $0.75$ . In many experiments the density in pulsed supersonic beams was found to be lower by up to an order of magnitude with respect to predictions assuming an ideal expansion, see for instance.<sup>99,129</sup> In experiments the source parameters are optimized for the total number of decelerated particles. Therefore, even if the relative transmission is lower, it may still be advantageous to operate the source at higher stagnation pressure to obtain the highest density of decelerated particles.

## 4 Applications

Cold gas-phase samples prepared by deceleration of pulsed supersonic beams are relevant to a range of applications including (i) precision spectroscopic measurements, (ii) the determination of lifetimes and decay processes of excited states, (iii) investigations of interactions with blackbody radiation, and (iv) studies of inelastic and reactive scattering. Experiments that have been carried out in each of these areas are described in the following, along with an outline of potential future developments.

### 4.1 Precision spectroscopic studies

With the narrow bandwidths and high frequency stability that are currently achievable with laser and micro-wave/millimetre-wave sources, the experimental resolution attained in precision spectroscopic measurements is in many cases limited by the interaction time between the atomic or molecular sample under investigation and the radiation field. It is therefore desirable to prepare samples of the relevant species in traps or in low-velocity beams. This is evident in vacuum-ultraviolet–millimetre-wave double-resonance experiments directed toward studying the role of nuclear spins in photoionization and precision measurements of importance in the accurate determination of ionization and dissociation energies.<sup>130</sup> Such measurements are currently limited to a resolution of  $60 \text{ kHz}$ <sup>131</sup> by the transit time of the atoms or molecules through the measurement region. The need for slow beams also arises in the high precision measurements of the  $1\text{S}\text{--}2\text{S}$  transition in atomic hydrogen by Hänsch and co-workers where currently the maximum achievable resolution is interaction-time limited.<sup>132,133</sup>

From the perspective of maximizing the effective measurement time and therefore the experimental resolution, precision microwave spectroscopic measurements on slow, quantum-state-selected beams of  $^{15}\text{ND}_3$  molecules prepared by multistage Stark deceleration have been demonstrated by van Veldhoven *et al.*<sup>134</sup> These measurements were performed on decelerated beams with velocities as low as  $50 \text{ m s}^{-1}$  which, upon traversal of a  $65 \text{ mm}$  long microwave radiation zone, led to the possibility of measuring the hyperfine-resolved inversion spectrum of  $^{15}\text{ND}_3$  with line-widths on the order of  $1 \text{ kHz}$ . Similar measurements of the Zeeman effect on the hyperfine structure of the  $^2\Pi_{3/2}$  ground state of the OH radical in weak magnetic fields have been performed by Lev *et al.*<sup>135</sup> These measurements relied on multistage Stark deceleration of the OH radicals to velocities of  $200 \text{ m s}^{-1}$  in the laboratory frame resulting in line widths of a few kHz under the experimental conditions. In addition to the benefits of enhanced interaction times, the measurements also gain from the state-selectivity of the multistage Stark decelerator, and the possibilities to focus the decelerated packets of molecules in the longitudinal and transverse dimensions.

Precision measurements are not only of importance to the determination of molecular structure and dynamics, but are also of value in placing constraints on the time-variation of fundamental constants including the fine-structure constant<sup>136,137</sup> and the proton-to-electron mass ratio.<sup>9,138</sup> The time-variation of these constants, which determine the

strength of the electromagnetic interaction, and the relative strength of the strong and electroweak interactions, could point toward physics beyond the standard model of particle physics. Such possibilities to exploit precision spectroscopic measurements of small molecules in the search for physics beyond the standard model are also key to experiments directed toward the search for an electric dipole moment (EDM) of the electron and the measurement of parity-violating energy differences between enantiomeric forms of chiral molecules.<sup>7,8</sup> Early experiments to place an upper limit on the size of the electron EDM were performed on atomic thallium,<sup>139</sup> however more recently the focus has been placed on polar diatomic molecules in which the sensitivity to an electron EDM is enhanced. Relevant molecules include YbF<sup>140</sup> and PbO,<sup>141</sup> with the most recent measurement to place a new upper limit on the size of the electron EDM performed using YbF.<sup>142</sup> The possibility to prepare high-density, velocity controlled, state-selected samples of these species to further improve the measurement precision have been envisaged. Multistage Stark deceleration of chiral molecules is also planned to measure parity violating energy differences using microwave spectroscopy.<sup>8</sup>

Because the low-lying states of heavy polar molecules are only very weakly low-field seeking, these experiments have provided particular motivation for the development of multi-stage Stark deceleration methods for molecules in high-field-seeking states.<sup>57,83</sup> Alternatively, the use of chip based decelerators<sup>15</sup> or long ring-decelerators<sup>69</sup> with their continuously moving minima represent approaches to decelerate molecules of this kind using sufficiently weak fields that the low-field-seeking states could be exploited. Although some of these molecules have strong electron Zeeman effects and are therefore amenable to multistage Zeeman deceleration, their large masses and the desire to minimize stray magnetic fields in the experiments makes this approach challenging. Rydberg–Stark deceleration following the photoexcitation of long-lived high- $\ell$  Rydberg states of these heavy, polar, diatomic molecules using the techniques described in Section 2.3 for the deceleration of H<sub>2</sub> also represents a potential approach to the production of velocity-controlled samples. However, it will necessitate efficient optical transfer from the Rydberg states to the relevant ro-vibronic states after deceleration.

## 4.2 Determination of excited state lifetimes

The possibility to electrically or magnetically trap samples after multistage deceleration or Rydberg–Stark deceleration has given rise to opportunities for the precise determination of lifetimes of excited states of atoms or molecules. The deceleration and electrostatic trapping of OH radicals following multistage Stark deceleration, first demonstrated by van de Meerakker *et al.*,<sup>143</sup> led to the possibility of studying the vibrational relaxation of the upper, low-field-seeking  $\Lambda$ -doublet component of the X<sup>2</sup> $\Pi_{3/2}$ ,  $v = 1$ ,  $J = 3/2$  level over timescales of several hundred milliseconds.<sup>144</sup> The radiative lifetime measured was  $59.0 \pm 2.0$  ms, in very good agreement with theoretical predictions of  $58.0 \pm 1.0$  ms which accounted for the effect of the electric field of the trap. In these experiments, the molecules were prepared in the  $v = 1$  state by optical pumping from the  $v = 0$  state prior to deceleration, with reference

measurements of the trap lifetime made with molecules in the  $v = 0$  state. Later, a combined experimental and theoretical study of the lifetime of CO in the metastable a<sup>3</sup> $\Pi$ ,  $v = 0$  state was also performed, by Gilijamse *et al.*,<sup>68</sup> using an electric quadrupole trap loaded following multistage Stark deceleration. In this case, the upper  $\Lambda$ -doublet component of the  $\Omega = 1$ ,  $v = 0$ ,  $J = 1$  and the  $\Omega = 2$ ,  $v = 0$ ,  $J = 2$  levels were each prepared by laser excitation from the ground state before deceleration. A comparison could then be made between the measured lifetimes of each of these states,  $2.63 \pm 0.03$  ms and  $140 \pm 4$  ms, respectively, with very good agreement found with theoretical predictions.

Both of these measurements demonstrate the way in which trapped samples can be exploited to perform lifetime measurements on timescales which, without trapping, would be very difficult to achieve. A similar situation arises in the case of long-lived Rydberg states of high principal quantum number, where processes such as predissociation and autoionization can compete with spontaneous emission to affect the lifetimes. The demonstration of three-dimensional electrostatic trapping of hydrogen Rydberg atoms was the first step toward studies of this kind.<sup>93</sup> In these Rydberg atom trapping experiments several processes contribute to the decay of atoms from the trap. These include collisions between the trapped atoms and the undecelerated, trailing edge of the gas pulse, collisions between the trapped atoms themselves, ionization by blackbody radiation and spontaneous emission toward the ground state. With the aim of disentangling these processes, the initial electrode configuration designed for deceleration and electrostatic trapping on the axis of the atomic beam was further developed to allow the adiabatic transfer of atoms away from the beam axis to an off-axis three-dimensional electrostatic trap. The possibility to eliminate collisional losses with particles in the trailing edge of the atomic beam, along with the reduction of the blackbody temperature to  $\sim 125$  K by cooling the electrodes, has provided direct insight into each of these trap loss mechanisms. This has indicated that after avoiding collisional losses at early times, ionization by blackbody radiation is the next most significant trap loss process at room temperature. Magnetic trapping after multistage Zeeman deceleration,<sup>85,87</sup> demonstrated with the example of magnetic trapping deuterium atoms in Fig. 8, also opens up the possibility of performing similar lifetime measurements on radicals with no permanent electric dipole moment in the ground state. Species of fundamental importance for which measurements of this kind would be of value include metastable states of H<sub>2</sub>, He<sub>2</sub> and N<sub>2</sub>.

Presented in Fig. 9 are a set of measurements of trap decay times for Rydberg states of atomic hydrogen with principal quantum numbers  $n = 32$  and  $n = 36$ . These experiments were performed in an off-axis electrostatic trap with a non-zero electric field minimum, at a blackbody temperature of  $\sim 125$  K.<sup>63</sup> Under these conditions, losses by collisions with the undecelerated, trailing edge of the atomic beam are minimized along with losses by ionization of the Rydberg atoms by blackbody radiation. However, even at  $\sim 125$  K, the rate of blackbody transitions between Rydberg states is significant with the result that after long trapping times the atoms that remain in the trap are distributed over Rydberg

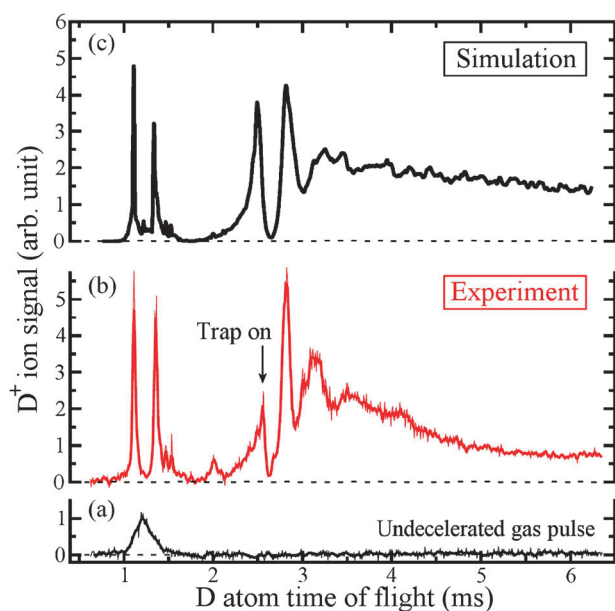


**Fig. 8** Magnetic trapping deuterium atoms after multistage Zeeman deceleration. Time-of-flight measurements of (a) the undecelerated beam of deuterium atoms, and (b) decelerated and trapped deuterium atoms. (c) Particle trajectory simulation of the complete deceleration and trapping process.

states with a range of principal quantum numbers, with states of lower  $n$  decaying toward the ground state more rapidly and those of higher  $n$  remaining trapped for longer times. The solid curves associated with each set of data in Fig. 9 are the result of a Monte-Carlo calculation of the trap decay rate including the effects of blackbody radiation and spontaneous emission and capture well the main features of the decay. An understanding of the effect of 300 K blackbody radiation on the lifetimes of Rydberg states of atomic hydrogen is of value in the interpretation of H atom photofragmentation translational spectra recorded by Rydberg tagging.<sup>145</sup>

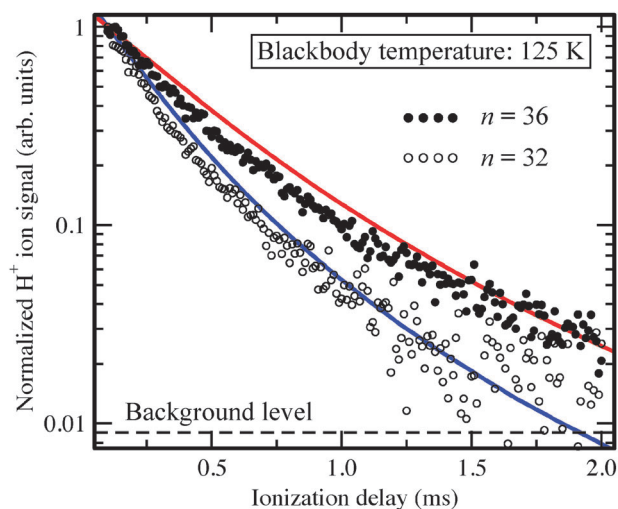


**Fig. 9** Measurements of the decay of electrostatically trapped hydrogen Rydberg atoms with principal quantum numbers  $n = 32$  (open circles, blue) and  $n = 36$  (full circles, red) recorded at a blackbody temperature of  $\sim 125$  K (adapted from Seiler *et al.*).<sup>63</sup>

These measurements on atomic hydrogen indicate that lower blackbody temperatures are required to disentangle the more complex decay processes that occur in molecular Rydberg states. For this reason a three-dimensional off-axis electrostatic Rydberg molecule trap which can be cooled to 4 K is now being developed at ETH Zurich. It is planned to employ this trap to study slow predissociation in non-penetrating Rydberg states of molecular hydrogen.

Because of the very large dipole moments associated with transitions between Rydberg states, which scale as  $n^2$ , they are very well suited to measuring blackbody temperatures.<sup>146,147</sup> The possibility to trap polar molecules on long timescales in electrostatic traps has also permitted the observation of optical pumping of trapped ground state OH radicals by blackbody radiation. These blackbody transitions between rotational states have rates on the order of  $0.1 \text{ s}^{-1}$  and therefore require trapping times on the order of several seconds for efficient observation as shown by Hoekstra *et al.*<sup>148</sup> for ground state OH and OD.

### 4.3 Collision studies

**4.3.1 Inelastic scattering.** The control over the velocity distributions of samples prepared by deceleration of pulsed supersonic beams is also of value to the study of collisions at low temperature or with a high degree of control over the kinetic energies of the colliding partners. The state-selective aspect of these techniques is of particular importance in the study of state-to-state inelastic scattering. From this perspective, velocity controlled beams of OH radicals prepared by multistage Stark deceleration were first used by Gilijamse *et al.* to study collisions with supersonic beams of ground-state xenon atoms.<sup>65</sup> These experiments were carried out in a crossed beam geometry in which the centre-of-mass collision energy could be tuned from  $\sim 50 \text{ cm}^{-1}$  to  $\sim 400 \text{ cm}^{-1}$ , with an energy resolution of  $\sim 13 \text{ cm}^{-1}$  and a minimum collision energy limited by the contribution of the undecelerated xenon beam. Over this energy range, thresholds for the onset of collisional excitation of low-lying rotational states could be resolved with state-selective detection performed by laser-induced fluorescence.

These crossed-beam collision studies using decelerated samples carried out in the absence of external fields were then followed by studies of collisions between magnetically trapped OH radicals and supersonic beams of helium and  $\text{D}_2$  by Sawyer *et al.*<sup>149</sup> In this work, the OH radicals were loaded into a magneto-electrostatic trap after multistage Stark deceleration with the electric fields of the trap then switched off before collisions between the magnetically trapped molecules and the beams of helium and  $\text{D}_2$  took place. Rather than tuning the collision energy by scanning the output velocity of the Stark decelerator, as was done in the earlier work of Gilijamse *et al.*, in these experiments the kinetic energies of the helium and  $\text{D}_2$  beams were tuned by adjusting the temperature at which the pulsed valve was operated. Collision rates and corresponding collision cross-sections were then determined by measuring trap loss rates. The energy level structure of the OH radicals in these experiments was significantly affected by the presence of the trapping magnetic fields which required a



detailed theoretical treatment including these fields for accurate interpretation of the experimental data.<sup>150</sup>

More recently a study of the OH–He and OH–D<sub>2</sub> collision systems was carried out by Kirste *et al.* in a crossed beam geometry in the absence of external fields.<sup>151</sup> These experiments permitted the determination of relative parity-resolved state-to-state inelastic scattering cross sections, which in the case of OH–He, allowed comparison with computed cross sections. In the case of OH–D<sub>2</sub>, no effects were observed on the cross sections that could be attributed to the rotational degrees of freedom of the D<sub>2</sub> molecule. These two examples of studies of low-energy collisions, with trapped samples and in crossed-beam geometries under field-free conditions, highlight the complications in the interpretation of the data recorded in the presence of the trapping fields. However, for processes with very small cross sections the benefits of the long interaction times that can be achieved with trapped samples are particularly valuable. High-order multipole electric or magnetic traps, with their flat-bottom field distributions, would therefore be well suited for experiments of this kind.

Collision experiments with multistage Stark decelerated OH radicals and Ar atoms have recently been studied in great detail by Scharfenberg *et al.*<sup>152</sup> In this work, which provides a benchmark in the scattering of open-shell molecules with atoms, the threshold behavior and collision-energy dependence of 13 inelastic scattering channels could be precisely determined. The level of sensitivity that was achieved in these experiments, to processes with cross sections  $\leq 0.01 \text{ \AA}^2$ , highlights the potential for further precision collision measurements which could be carried out with Stark- and Zeeman-decelerated molecular beams. The possibility to confine decelerated samples to orbit in a ring,<sup>153–155</sup> providing the opportunity to extend interaction times, may also be valuable in further improving sensitivity.

**4.3.2 Reactive scattering.** The high densities and low temperatures in supersonic beams have been used for some time in studies of reactive scattering. The technique known as CRESU (Cinétique de Réaction en Ecoulement Supersonique Uniforme, or Reaction Kinetics in Uniform Supersonic Flow) employs the supersonic expansion from a Laval nozzle to produce a flow of gas that is uniform in temperature and density.<sup>156,157</sup> Such expansions have permitted experimental studies of reactions such as  $\text{OH} + \text{HBr} \rightarrow \text{H}_2\text{O} + \text{Br}$  at temperatures on the order of  $\sim 10 \text{ K}$  with recent studies of the  $\text{S} + \text{H}_2 \rightarrow \text{SH} + \text{H}$  reactions carried out at temperatures down to  $5.8 \text{ K}$ .<sup>158,159</sup>

As temperatures, or collision energies, are reduced to below those achievable using CRESU, scattering events begin to be dominated by individual angular momentum partial waves, and quantum effects such as tunneling start to play an important role. For reactions involving light species such as  $\text{H}_2$ , these effects can occur at temperatures of about  $0.5 \text{ K}$ , for example in the reaction of  $\text{F} + \text{H}_2 \rightarrow \text{HF} + \text{H}$ .<sup>160</sup> For reactions involving heavier samples, lower temperatures are necessary before tunneling becomes important.

Ion–molecule reactive scattering experiments have been carried out by Willitsch *et al.* at temperatures approaching  $1 \text{ K}$ . In this work the temperature dependence of the rate

constant was determined for the  $\text{Ca}^+ + \text{CH}_3\text{F} \rightarrow \text{CaF}^+ + \text{CH}_3$  reaction.<sup>27</sup> Velocity selection from an effusive source<sup>31</sup> was used to produce the translationally cold  $\text{CH}_3\text{F}$  for these studies. In a second generation of these experiments, it is foreseen to exploit the quantum-state-selection and tunable collision energies achievable by multistage Stark or Zeeman deceleration of pulsed supersonic beams to enter a still lower temperature regime.

**4.3.3 Collisions with surfaces.** The interaction of a Rydberg atom or molecule with a metal surface represents a model system for studies of electron transfer, as tunnel ionization of the Rydberg electron into the conduction band of the metal is the dominant process that occurs at short range. Several studies of collisional ionization at grazing incidence to atomically flat gold surfaces have been performed by Dunning and co-workers<sup>161,162</sup> and Softley and co-workers.<sup>163</sup> These experiments have involved beams of xenon and molecular hydrogen excited to Rydberg states, with more recent work emphasizing the importance of studies using atomic hydrogen.<sup>164</sup> Experiments of this kind with atomic hydrogen benefit from the possibility to precisely calculate ionization fields and rates, but difficulties arise when using beams of atomic hydrogen produced by photolysis of a precursor molecule such as  $\text{NH}_3$ . In such cases the precursor can be adsorbed on the surface, modifying the atom–surface interaction potential of interest. For this reason the techniques developed to adiabatically guide a beam of Rydberg atoms away from the molecular beam axis for off-axis trapping<sup>63</sup> may also be of importance for Rydberg-surface collision studies.

## 5 Conclusion

The deceleration of supersonic beams using time-dependent inhomogeneous electric and magnetic fields represents a very attractive method of producing slow beams of cold atoms and molecules and, if desired, loading the cold samples into electric or magnetic traps. This article has presented an overview of research related to the production and use of such samples in experiments in atomic and molecular physics. Multistage Stark deceleration was developed first<sup>56</sup> and is particularly well suited for molecules having a large permanent dipole moment. Multistage Zeeman deceleration, its magnetic analogue, can be used to decelerate paramagnetic atoms and molecules. Rydberg Stark deceleration is, in principle, applicable to any gas-phase species and benefits from the advantages of extremely large dipole moments but necessitates the use of lasers to prepare the Rydberg states and, if required, pump them down to the ground state following deceleration. These three related methods offer considerable flexibility in the manipulation of the translational motion of a wide range of molecules, and first real applications in high-resolution spectroscopy and reaction dynamics are becoming possible. At present, the phase-space densities that can be reached are not sufficient to implement further cooling steps, but in future the implementation of continuous trap loading and optical cooling schemes<sup>32–34,165–170</sup> in combination with deceleration techniques appears promising.



## Acknowledgements

This work is supported by the Swiss National Science Foundation (Project No. 200020-132688) and the European Research Council advanced grant program (Project No. 228286). M. M. thanks ETH Zürich for the support through an ETH fellowship.

## References

- 1 D. Herschbach, *Faraday Discuss.*, 2009, **142**, 9–23.
- 2 M. T. Bell and T. P. Softley, *Mol. Phys.*, 2009, **107**, 99–132.
- 3 S. Ospelkaus, K.-K. Ni, M. H. G. de Miranda, B. Neyenhuis, D. Wang, S. Kotochigova, P. S. Julienne, D. S. Jin and J. Ye, *Faraday Discuss.*, 2009, **142**, 351–359.
- 4 K.-K. Ni, S. Ospelhaus, D. J. Nesbitt, J. Ye and D. S. Jin, *Phys. Chem. Chem. Phys.*, 2009, **11**, 9626–9639.
- 5 R. V. Krems, *Phys. Chem. Chem. Phys.*, 2008, **10**, 4079–4092.
- 6 M. R. Tarbutt, J. J. Hudson, B. E. Sauer and E. A. Hinds, in *Cold Molecules: Theory, Experiment, Applications*, ed. R. V. Krems, W. C. Stwalley and B. Friedrich, CRC Press, Boca Raton, 2009.
- 7 M. Quack, J. Stohner and M. Willeke, *Annu. Rev. Phys. Chem.*, 2008, **59**, 741.
- 8 M. Schnell and J. Küpper, *Faraday Discuss.*, 2011, **150**, 33.
- 9 H. L. Bethlem and W. Ubachs, *Faraday Discuss.*, 2009, **142**, 25–36.
- 10 T. F. Gallagher and P. Pillet, *Adv. At., Mol., Opt. Phys.*, 2008, **56**, 161.
- 11 T. Wilk, A. Gaëtan, C. Evellin, J. Wolters, Y. Miroshnychenko, P. Grangier and A. Browaeys, *Phys. Rev. Lett.*, 2010, **104**, 010502.
- 12 L. Isenhower, E. Urban, X. L. Zhang, A. T. Gill, T. Henage, T. A. Johnson, T. G. Walker and M. Saffman, *Phys. Rev. Lett.*, 2010, **104**, 010503.
- 13 J. Mozley, P. Hyafil, G. Nogues, M. Brune, J.-M. Raimond and S. Haroche, *Eur. Phys. J. D*, 2005, **35**, 43–57.
- 14 A. Emmert, A. Lupascu, G. Nogues, M. Brune, J.-M. Raimond and S. Haroche, *Eur. Phys. J. D*, 2009, **51**, 173–177.
- 15 S. A. Meek, H. Conrad and G. Meijer, *Science*, 2009, **324**, 1699–1702.
- 16 H. L. Bethlem and G. Meijer, *Int. Rev. Phys. Chem.*, 2003, **22**, 73–128.
- 17 T. P. Softley, *Int. Rev. Phys. Chem.*, 2004, **23**, 1–78.
- 18 S. D. Hogan, E. Vliegen, D. Sprecher, N. Vanhaecke, M. Andrist, H. Schmutz, U. Meier, B. H. Meier and F. Merkt, in *Laser Spectroscopy*, Proceedings of the XVIII International Conference ICOLS 2007, ed. L. Hollberg, J. Bergquist and M. Kasevich, Singapore, 2008, pp. 153–166.
- 19 B. Friedrich and J. M. Doyle, *ChemPhysChem*, 2009, **10**, 604.
- 20 M. Schnell and G. Meijer, *Angew. Chem., Int. Ed.*, 2009, **48**, 6010–6031.
- 21 L. C. Carr, D. DeMille, R. V. Krems and J. Ye, *New J. Phys.*, 2009, **11**, 055049.
- 22 A. Fioretti, D. Comparat, A. Crubellier, O. Dulieu, F. Masnou-Séeuws and P. Pillet, *Phys. Rev. Lett.*, 1998, **80**, 4402–4405.
- 23 S. Jochim, M. Bartenstein, A. Altmeyer, G. Hendl, S. Riedl, C. Chin, J. Hecker-Denschlag and R. Grimm, *Science*, 2003, **302**, 2101–2103.
- 24 M. Greiner, C. A. Regall and D. S. Jin, *Nature*, 2003, **426**, 537–540.
- 25 J. M. Doyle, B. Friedrich, J. Kim and D. Patterson, *Phys. Rev. A: At., Mol., Opt. Phys.*, 1995, **52**, R2515–R2518.
- 26 P. F. Staunum, K. Højbjerg, R. Wester and M. Drewsen, *Phys. Rev. Lett.*, 2008, **100**, 243003.
- 27 S. Willitsch, M. T. Bell, A. D. Gingell, S. R. Procter and T. P. Softley, *Phys. Rev. Lett.*, 2008, **100**, 043203.
- 28 X. Tong, A. H. Winney and S. Willitsch, *Phys. Rev. Lett.*, 2010, **105**, 143001.
- 29 R. Fulton, A. I. Bishop and P. F. Barker, *Phys. Rev. Lett.*, 2004, **93**, 243004.
- 30 M. Gupta and D. Herschbach, *J. Phys. Chem. A*, 2001, **105**, 1626–1637.
- 31 S. A. Rangwala, T. Junglen, T. Rieger, P. W. H. Pinkse and G. Rempe, *Phys. Rev. A: At., Mol., Opt. Phys.*, 2003, **67**, 043406.
- 32 E. S. Shuman, J. F. Barry and D. DeMille, *Nature*, 2010, **467**, 820–823.
- 33 P. F. Staunum, K. Højbjerg, P. S. Skyt, A. K. Hansen and M. Drewsen, *Nat. Phys.*, 2010, **6**, 271–274.
- 34 T. Schneider, B. Roth, H. Duncker, I. Ernsting and S. Schiller, *Nat. Phys.*, 2010, **6**, 275.
- 35 P. F. Barker and M. N. Shneider, *Phys. Rev. Lett.*, 2002, **66**, 065402.
- 36 P. F. Barker, S. M. Purcell, P. Douglas, P. Barletta, N. Coppendale, C. Maher-McWilliams and J. Tennyson, *Faraday Discuss.*, 2009, **142**, 175.
- 37 O. Stern, *Z. Phys.*, 1921, **7**, 249–253.
- 38 W. Gerlach and O. Stern, *Z. Phys.*, 1921, **8**, 110–111.
- 39 W. Gerlach and O. Stern, *Z. Phys.*, 1922, **9**, 349–352.
- 40 W. Gerlach and O. Stern, *Z. Phys.*, 1922, **9**, 353–355.
- 41 W. Gerlach, *Ann. Phys.*, 1925, **381**, 163.
- 42 I. I. Rabi, J. R. Zacharias, S. Millman and P. Kusch, *Phys. Rev.*, 1938, **53**, 318.
- 43 I. I. Rabi, S. Millman, P. Kusch and J. R. Zacharias, *Phys. Rev.*, 1939, **55**, 526.
- 44 F. Bloch and I. I. Rabi, *Rev. Mod. Phys.*, 1945, **17**, 237.
- 45 J. W. Emsley and J. Feeney, *Prog. Nucl. Magn. Reson. Spectrosc.*, 2007, **50**, 179.
- 46 A. Kantrowitz and J. Grey, *Rev. Sci. Instrum.*, 1951, **22**, 328.
- 47 E. W. Becker and K. Bier, *Z. Naturforsch.*, 1954, **9**, 975.
- 48 R. E. Smalley, L. Wharton and D. H. Levy, *Acc. Chem. Res.*, 1977, **10**, 139.
- 49 R. D. Levine and R. B. Bernstein, *Molecular Reaction Dynamics and Chemical Reactivity*, Oxford University Press, New York, 1987.
- 50 *Atomic and molecular beam methods*, ed. G. Scoles, Oxford University Press, New York, 1988–1992.
- 51 H. G. Bennewitz, W. Paul and Ch. Schlier, *Z. Phys.*, 1955, **141**, 6.
- 52 J. P. Gordon, H. J. Zeiger and C. H. Townes, *Phys. Rev.*, 1955, **99**, 1264.
- 53 P. R. Brooks, *Science*, 1976, **193**, 11–16.
- 54 S. Stolte, *Ber. Bunsenges. Phys. Chem.*, 1982, **86**, 413–421.
- 55 D. H. Parker and R. B. Bernstein, *Annu. Rev. Phys. Chem.*, 1989, **40**, 561–595.
- 56 H. L. Bethlem, G. Berden and G. Meijer, *Phys. Rev. Lett.*, 1999, **83**, 1558–1561.
- 57 H. L. Bethlem, F. M. H. Crompvoets, R. T. Jongma, S. Y. T. van de Meerakker and G. Meijer, *Phys. Rev. A: At., Mol., Opt. Phys.*, 2002, **65**, 053416.
- 58 S. Y. T. van de Meerakker, H. L. Bethlem and G. Meijer, *Nat. Phys.*, 2008, **4**, 595.
- 59 N. Vanhaecke, U. Meier, M. Andrist, B. H. Meier and F. Merkt, *Phys. Rev. A: At., Mol., Opt. Phys.*, 2007, **75**, 031402(R).
- 60 E. Narevicius, A. Libson, C. G. Parthey, I. Chavez, J. Narevicius, U. Even and M. G. Raizen, *Phys. Rev. Lett.*, 2008, **100**, 093003.
- 61 S. R. Procter, Y. Yamakita, F. Merkt and T. P. Softley, *Chem. Phys. Lett.*, 2003, **374**, 667–675.
- 62 E. Vliegen, H. J. Wörner, T. P. Softley and F. Merkt, *Phys. Rev. Lett.*, 2004, **92**, 033005.
- 63 Ch. Seiler, S. D. Hogan, H. Schmutz, J. A. Agner and F. Merkt, *Phys. Rev. Lett.*, 2011, **106**, 073003.
- 64 E. Vliegen and F. Merkt, *Phys. Rev. Lett.*, 2006, **97**, 033002.
- 65 J. J. Gilijamse, S. Hoekstra, S. Y. T. van de Meerakker, G. C. Groenenboom and G. Meijer, *Science*, 2006, **313**, 1617.
- 66 A. Kellerbauer, M. Amoretti, A. Belov, G. Bonomi, I. Boscolo, R. Brusa, M. Büchner, V. Byakov, L. Cabaret, C. Canali, C. Carraro, F. Castelli, S. Cialdi, M. de Combarieu, D. Comparat, G. Consolati, N. Djourellov, M. Doser, G. Drobychev, A. Dupasquier, G. Ferrari, P. Forget, L. Formaro, A. Gervasini, M. Giammarchi, S. Gninenko, G. Gribakin, S. D. Hogan, M. Jacquy, V. Lagomarsino, G. Manuzio, S. Mariazzi, V. Matveev, J. Meier, F. Merkt, P. Nedelec, M. Oberthaler, P. Pari, M. Prevedelli, F. Quasso, A. Rotondi, D. Sillou, S. Stepanov, H. Stroke, G. Testera, G. Tino, G. Tréneç, A. Vairo, J. Vigué, H. Walters, U. Warring, S. Zavatarelli and D. Zvezhinskij, *Nucl. Instrum. Methods Phys. Res., Sect. B*, 2008, **266**, 351–356.
- 67 H. L. Bethlem, A. van Roij, R. T. Jongma and G. Meijer, *Phys. Rev. Lett.*, 2002, **88**, 133003.
- 68 J. J. Gilijamse, S. Hoekstra, S. A. Meek, M. Metsälä, S. Y. T. van de Meerakker, G. Meijer and G. C. Groenenboom, *J. Chem. Phys.*, 2007, **127**, 221102.

- 69 A. Osterwalder, S. A. Meek, G. Hammer, H. Haak and G. Meijer, *Phys. Rev. A: At., Mol., Opt. Phys.*, 2010, **81**, 051401(R).
- 70 A. Marian, H. Haak, P. Geng and G. Meijer, *Eur. Phys. J. D*, 2010, **59**, 179.
- 71 H. L. Bethlem, G. Berden, F. M. H. Crompvoets, R. T. Jongma, A. J. A. van Roij and G. Meijer, *Nature*, 2000, **406**, 491.
- 72 J. van Veldhoven, H. L. Bethlem and G. Meijer, *Phys. Rev. Lett.*, 2005, **94**, 083001.
- 73 J. R. Bochinski, E. R. Hudson, H. J. Lewandowski, G. Meijer and J. Ye, *Phys. Rev. Lett.*, 2003, **91**, 243001.
- 74 S. Y. T. van de Meerakker, P. H. M. Smeets, N. Vanhaecke, R. T. Jongma and G. Meijer, *Phys. Rev. Lett.*, 2005, **94**, 023004.
- 75 B. C. Sawyer, B. L. Lev, E. R. Hudson, B. K. Stuhl, M. Lara, J. L. Bohn and J. Ye, *Phys. Rev. Lett.*, 2007, **98**, 253002.
- 76 O. Bucicov, M. Nowak, S. Jung, G. Meijer, E. Tiemann and C. Lisdat, *Eur. Phys. J. D*, 2008, **46**, 463–469.
- 77 E. R. Hudson, C. Ticknor, B. C. Sawyer, C. A. Taatjes, H. J. Lewandowski, J. R. Bochinski, J. L. Bohn and J. Ye, *Phys. Rev. A: At., Mol., Opt. Phys.*, 2006, **73**, 063404.
- 78 S. Y. T. van de Meerakker, I. Labazan, S. Hoekstra, J. Küpper and G. Meijer, *J. Phys. B: At., Mol. Opt. Phys.*, 2006, **39**, S1077.
- 79 S. Hoekstra, M. Metsälä, P. C. Zieger, L. Scharfenberg, J. J. Gilijamse, G. Meijer and S. Y. T. van de Meerakker, *Phys. Rev. A: At., Mol., Opt. Phys.*, 2007, **76**, 063408.
- 80 S. K. Tokunaga, J. M. Dyne, E. A. Hinds and M. R. Tarbutt, *New J. Phys.*, 2009, **11**, 055038.
- 81 T. E. Wall, S. K. Tokunaga, E. A. Hinds and M. R. Tarbutt, *Phys. Rev. A: At., Mol., Opt. Phys.*, 2010, **81**, 033414.
- 82 T. E. Wall, J. F. Kanem, J. M. Dyne, J. J. Hudson, B. E. Sauer, E. A. Hinds and M. R. Tarbutt, *arXiv.org:1104.3976v1*, 2011.
- 83 M. R. Tarbutt, H. L. Bethlem, J. J. Hudson, V. L. Ryabov, V. A. Ryzhov, B. E. Sauer, G. Meijer and E. A. Hinds, *Phys. Rev. Lett.*, 2004, **92**, 173002.
- 84 K. Wohlfart, F. Grätz, F. Filsinger, H. Haak, G. Meijer and J. Küpper, *Phys. Rev. A: At., Mol., Opt. Phys.*, 2008, **77**, 031404.
- 85 S. D. Hogan, A. W. Wiederkehr, H. Schmutz and F. Merkt, *Phys. Rev. Lett.*, 2008, **101**, 143001.
- 86 S. D. Hogan, D. Sprecher, M. Andrist, N. Vanhaecke and F. Merkt, *Phys. Rev. A: At., Mol., Opt. Phys.*, 2007, **76**, 023412.
- 87 A. W. Wiederkehr, S. D. Hogan, B. Lambillotte, M. Andrist, H. Schmutz, J. Agner, Y. Salathé and F. Merkt, *Phys. Rev. A: At., Mol., Opt. Phys.*, 2010, **81**, 021402(R).
- 88 A. Trimeche, M. Bera, J. Cromières, J. Robert and N. Vanhaecke, *Eur. Phys. J. D*, 2011, DOI: 10.1140/epjd/e2011-20048.
- 89 E. Narevicius, A. Libson, C. G. Parthey, I. Chavez, J. Narevicius, U. Even and M. G. Raizen, *Phys. Rev. A: At., Mol., Opt. Phys.*, 2008, **77**, 051401.
- 90 E. Vliegen and F. Merkt, *J. Phys. B: At., Mol. Opt. Phys.*, 2005, **38**, 1623–1636.
- 91 E. Vliegen and F. Merkt, *J. Phys. B: At., Mol. Opt. Phys.*, 2006, **39**, L241–L247.
- 92 E. Vliegen, S. D. Hogan, H. Schmutz and F. Merkt, *Phys. Rev. A: At., Mol., Opt. Phys.*, 2007, **76**, 023405.
- 93 S. D. Hogan and F. Merkt, *Phys. Rev. Lett.*, 2008, **100**, 043001.
- 94 S. D. Hogan, Ch. Seiler and F. Merkt, *Phys. Rev. Lett.*, 2009, **103**, 123001.
- 95 D. R. Miller, in *Atomic and molecular beam methods*, ed. G. Scoles, Oxford University Press, New York, 1988–1992.
- 96 J. B. Anderson and J. B. Fenn, *Phys. Fluids*, 1965, **8**, 780.
- 97 J. B. Anderson, in *Molecular Beams and Low Density Gas Dynamics*, ed. P. P. Wegener, Marcel Dekker Inc., New York, 1974, vol. 4, pp. 1–91.
- 98 D. H. Levy, *Annu. Rev. Phys. Chem.*, 1980, **31**, 197.
- 99 C. T. Rettner, E. E. Marinero, R. N. Zare and A. H. Kung, *J. Phys. Chem.*, 1984, **88**, 4459–4465.
- 100 H. Ashkenas and F. S. Sherman, *Rarefied Gas Dynamics. Proceedings of the 4th International Symposium 1964*, New York, 1966, vol. 2, pp. 84–105.
- 101 J. P. Toennies and K. Winkelmann, *J. Chem. Phys.*, 1977, **66**, 3965.
- 102 S. Willitsch, J. M. Dyke and F. Merkt, *Helv. Chim. Acta*, 2003, **86**, 1152–1166.
- 103 S. Y. T. van de Meerakker, N. Vanhaecke and G. Meijer, *Annu. Rev. Phys. Chem.*, 2006, **57**, 159.
- 104 H. Lewandowski, E. R. Hudson, J. Bochinski and J. Ye, *Chem. Phys. Lett.*, 2004, **395**, 53–57.
- 105 E. Narevicius, C. G. Parthey, A. Libson, J. Narevicius, I. Chavez, U. Even and M. G. Raizen, *New J. Phys.*, 2007, **9**, 358.
- 106 H. L. Bethlem, G. Berden, A. J. A. van Roij, F. M. H. Crompvoets and G. Meijer, *Phys. Rev. Lett.*, 2000, **84**, 5744–5747.
- 107 E. M. McMillan, *Phys. Rev.*, 1945, **68**, 143.
- 108 V. Veksler, *J. Phys. (USSR)*, 1945, **9**, 153–158.
- 109 A. W. Wiederkehr, S. D. Hogan and F. Merkt, *Phys. Rev. A: At., Mol., Opt. Phys.*, 2010, **82**, 043428.
- 110 S. D. Hogan, A. W. Wiederkehr, M. Andrist, H. Schmutz and F. Merkt, *J. Phys. B: At., Mol. Opt. Phys.*, 2008, **41**, 081005.
- 111 S. Y. T. van de Meerakker, N. Vanhaecke, H. L. Bethlem and G. Meijer, *Phys. Rev. A: At., Mol., Opt. Phys.*, 2006, **73**, 023401.
- 112 S. A. Meek, H. L. Bethlem, H. Conrad and G. Meijer, *Phys. Rev. Lett.*, 2008, **100**, 152003.
- 113 E. Lavert-Ofir, S. Gersten, A. B. Henson, I. Shani, L. David, J. Narevicius and E. Narevicius, *arXiv.org:1011.0418v2*, 2010.
- 114 T. F. Gallagher, *Rydberg Atoms*, Cambridge University Press, Cambridge, 1994.
- 115 Ch. Seiler, S. D. Hogan and F. Merkt, *Phys. Chem. Chem. Phys.*, 2011, DOI: 10.1039/c1cp21276a.
- 116 T. Breeden and H. Metcalf, *Phys. Rev. Lett.*, 1981, **47**, 1726–1729.
- 117 W. H. Wing, *Phys. Rev. Lett.*, 1980, **45**, 631–634.
- 118 D. Townsend, A. L. Goodgame, S. R. Procter, S. R. Mackenzie and T. P. Softley, *J. Phys. B: At., Mol. Opt. Phys.*, 2001, **34**, 439–450.
- 119 Y. Yamakita, S. R. Procter, A. L. Goodgame, T. P. Softley and F. Merkt, *J. Chem. Phys.*, 2004, **121**, 1419–1431.
- 120 E. Vliegen, P. Limacher and F. Merkt, *Eur. Phys. J. D*, 2006, **40**, 73–80.
- 121 Y. V. Gott, M. S. Ioffe and V. G. Tel'kovskii, *Nucl. Fusion Suppl.*, 1962, **Pt. 3**, 1045.
- 122 D. E. Pritchard, *Phys. Rev. Lett.*, 1983, **51**, 1336.
- 123 A. W. Wiederkehr, S. D. Hogan, M. Andrist, H. Schmutz and F. Merkt, *unpublished data*, 2009.
- 124 U. Even, J. Jortner, D. Noy, N. Lavie and C. Cossart-Magos, *J. Chem. Phys.*, 2000, **112**, 8068.
- 125 V. Aquilanti, D. Ascenzi, D. Cappelletti, S. Franceschini and F. Pirani, *Phys. Rev. Lett.*, 1995, **74**, 2929.
- 126 V. Aquilanti, D. Ascenzi, D. Cappelletti, M. de Castro and F. Pirani, *J. Chem. Phys.*, 1998, **109**, 3898.
- 127 R. B. Bernstein and K. H. Kramer, *J. Chem. Phys.*, 1963, **38**, 2507–2511.
- 128 R. B. Bernstein, *J. Chem. Phys.*, 1963, **38**, 2599.
- 129 A. H. Kung, *Opt. Lett.*, 1983, **8**, 24–26.
- 130 D. Sprecher, Ch. Jungen, W. Ubachs and F. Merkt, *Faraday Discuss.*, 2011, **150**, 51.
- 131 F. Merkt and A. Osterwalder, *Int. Rev. Phys. Chem.*, 2002, **21**, 385–403.
- 132 M. Niering, R. Holzwarth, J. Reichert, P. Pokasov, Th. Udem, M. Weitz, T. W. Hänsch, P. Lemonde, G. Santarelli, M. Abgrall, P. Laurent, C. Salomon and A. Clairon, *Phys. Rev. Lett.*, 2000, **84**, 5496.
- 133 C. G. Parthey, A. Matveev, J. Alnis, R. Pohl, Th. Udem, U. D. Jentschura, N. Kolachevsky and T. W. Hänsch, *Phys. Rev. Lett.*, 2010, **104**, 233001.
- 134 J. van Veldhoven, J. Küpper, H. L. Bethlem, B. Sartakov, A. J. A. van Roij and G. Meijer, *Eur. Phys. J. D*, 2004, **31**, 337–349.
- 135 B. L. Lev, E. R. Meyer, E. R. Hudson, B. C. Sawyer, J. L. Bohn and J. Ye, *Phys. Rev. A: At., Mol., Opt. Phys.*, 2006, **74**, 061402(R).
- 136 V. V. Flambaum and M. G. Kozlov, in *Cold Molecules: Theory, Experiment, Applications*, ed. R. V. Krems, W. C. Stwalley and B. Friedrich, CRC Press, Boca Raton, 2009.
- 137 E. R. Hudson, H. J. Lewandowski, B. C. Sawyer and J. Ye, *Phys. Rev. Lett.*, 2006, **96**, 143004.
- 138 S. Schiller and V. Korobov, *Phys. Rev. A: At., Mol., Opt. Phys.*, 2005, **71**, 032505.
- 139 B. C. Regan, E. D. Commins, Ch. J. Schmidt and D. DeMille, *Phys. Rev. Lett.*, 2002, **88**, 071805.
- 140 J. J. Hudson, B. E. Sauer, M. R. Tarbutt and E. A. Hinds, *Phys. Rev. Lett.*, 2002, **89**, 023003.

- 141 M. Kozlov and D. DeMille, *Phys. Rev. Lett.*, 2002, **89**, 133001.
- 142 J. J. Hudson, D. M. Kara, I. J. Smallman, B. E. Sauer, M. R. Tarbutt and E. A. Hinds, *Nature*, 2011, **473**, 493.
- 143 S. Y. T. van de Meerakker, P. H. M. Smeets, N. Vanhaecke, R. T. Jongma and G. Meijer, *Phys. Rev. Lett.*, 2005, **94**, 023004.
- 144 S. Y. T. van de Meerakker, N. Vanhaecke, M. P. J. van der Loo, G. Groenenboom and G. Meijer, *Phys. Rev. Lett.*, 2005, **95**, 013003.
- 145 M. N. R. Ashfold, G. A. King, M. G. D. Nix and T. A. A. Oliver, in *Handbook of High-Resolution Spectroscopy*, ed. M. Quack and F. Merkt, John Wiley & Sons, Chichester, 2011.
- 146 T. F. Gallagher and W. E. Cooke, *Phys. Rev. Lett.*, 1979, **42**, 835.
- 147 W. P. Spencer, A. G. Vaidyanathan, D. Kleppner and T. W. Ducas, *Phys. Rev. A: At., Mol., Opt. Phys.*, 1982, **25**, 380–384.
- 148 S. Hoekstra, J. J. Gilijamse, B. Sartakov, N. Vanhaecke, L. Scharfenberg, S. Y. T. van de Meerakker and G. Meijer, *Phys. Rev. Lett.*, 2007, **98**, 133001.
- 149 B. C. Sawyer, B. K. Stuhl, D. Wang, M. Yeo and J. Ye, *Phys. Rev. Lett.*, 2008, **101**, 173–177.
- 150 T. V. Tscherbul, Z. Pavlovic, H. R. Sadeghpour, R. Côté and A. Dalgarno, *Phys. Rev. A: At., Mol., Opt. Phys.*, 2010, **82**, 022704.
- 151 M. Kirste, L. Scharfenberg, J. Klos, F. Lique, M. H. Alexander, G. Meijer and S. Y. T. van de Meerakker, *Phys. Rev. A: At., Mol., Opt. Phys.*, 2010, **82**, 042717.
- 152 L. Scharfenberg, J. Klos, P. J. Dagdigan, M. H. Alexander, G. Meijer and S. Y. T. van de Meerakker, *Phys. Chem. Chem. Phys.*, 2010, **12**, 10660.
- 153 F. M. H. Crompvoets, H. L. Bethlem, R. T. Jongma and G. Meijer, *Nature*, 2001, **411**, 174.
- 154 C. E. Heiner, H. L. Bethlem and G. Meijer, *Phys. Chem. Chem. Phys.*, 2006, **8**, 2666.
- 155 P. C. Zieger, S. Y. T. van de Meerakker, C. E. Heiner, H. L. Bethlem, A. J. A. van Roij and G. Meijer, *Phys. Rev. Lett.*, 2010, **105**, 173001.
- 156 B. R. Rowe, G. Dupeyrat, J. B. Marquette and P. J. Gaucherel, *Chem. Phys.*, 1984, **80**, 4915.
- 157 G. Dupeyrat, J. B. Marquette and B. R. Rowe, *Phys. Fluids*, 1985, **28**, 1273.
- 158 I. W. M. Smith, *Chem. Rev.*, 2003, **103**, 4549.
- 159 C. Berteloite, M. Lara, A. Bergeat, S. D. L. Picard, F. Dayou, K. M. Hickson, A. Canosa, Ch. Naulin, J.-M. Launay, I. R. Sims and M. Costes, *Phys. Rev. Lett.*, 2010, **105**, 203201.
- 160 E. Bodo, F. A. Gianturco, N. Balakrishnan and A. Dalgarno, *J. Phys. B: At., Mol. Opt. Phys.*, 2004, **37**, 3641.
- 161 S. B. Hill, C. B. Haich, Z. Zhou, P. Nordlander and F. B. Dunning, *Phys. Rev. Lett.*, 2000, **85**, 5444.
- 162 D. D. Neufeld, H. R. Dunham, S. Wettkam, J. C. Lancaster and F. B. Dunning, *Phys. Rev. B: Condens. Matter Mater. Phys.*, 2008, **78**, 115423.
- 163 G. R. Lloyd, S. R. Procter and T. P. Softley, *Phys. Rev. Lett.*, 2005, **95**, 133202.
- 164 E. So, M. T. Bell and T. P. Softley, *Phys. Rev. A: At., Mol., Opt. Phys.*, 2009, **79**, 012901.
- 165 S. Y. T. van de Meerakker, R. T. Jongma, H. L. Bethlem and G. Meijer, *Phys. Rev. A: At., Mol., Opt. Phys.*, 2001, **64**, 041401.
- 166 M. D. Di Rosa, *Eur. Phys. J. D*, 2004, **31**, 395.
- 167 G. N. Price, S. T. Bannerman, K. Viering, E. Narevicius and M. G. Raizen, *Phys. Rev. Lett.*, 2008, **100**, 093004.
- 168 M. Zeppenfeld, M. Motsch, P. W. H. Pinkse and G. Rempe, *Phys. Rev. A: At., Mol., Opt. Phys.*, 2009, **80**, 041401(R).
- 169 M. Falkenau, V. V. Volchkov, J. Rührig, A. Griesmaier and T. Pfau, *Phys. Rev. Lett.*, 2011, **106**, 163002.
- 170 J. Riedel, S. Hoekstra, W. Jäger, J. J. Gilijamse, S. Y. T. van de Meerakker and G. Meijer, *Eur. Phys. J. D*, 2011, DOI: 10.1140/epjd/e2011-20082-7.